Materials & Design 208 (2021) 109908

Contents lists available at ScienceDirect

Materials & Design

journal homepage: www.elsevier.com/locate/matdes

High strain rate effect on tensile ductility and fracture of AM fabricated Inconel 718 with voided microstructures

P. Wood [a], A. Rusinek [b,d], P. Platek [c,*], J. Janiszewski [c], J. Sienkiewicz [c], U.F. Gunputh [a,*], K. Rajkowski [c], M.H. Miguélez [d]

[a] Institute of Innovation in Sustainable Engineering (IISE) University of Derby, Quaker Way, Derby DE1 3HD, UK
[b] Laboratory of Microstructure Studies and Mechanics of Materials (LEM3), Lorraine University, UMR CNRS 7239, 57078 Metz, France
[c] Faculty of Mechatronics, Armament and Aerospace, Military University of Technology, gen. Sylwestra Kaliskiego 2, 00 908 Warsaw, Poland
[d] Department of Mechanical Engineering, University Carlos III of Madrid, Avda. Universidad 30, 28911 Madrid, Spain

HIGHLIGHTS

- New empirical model to predict porosity type and growth rates in Inconel718.
- Model used to optimise laser melting process for Inconel718.
- Electromagnetic Ring Expansion Tests on additively manufactured Inconel718.
- Significant strain rate effects on alloy ductility observed together with new trends.

GRAPHICAL ABSTRACT

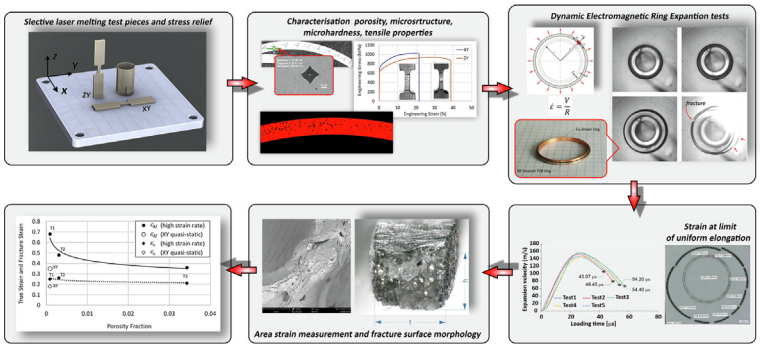

ARTICLE INFO

Article history:
Received 23 April 2021
Revised 12 June 2021
Accepted 15 June 2021
Available online 17 June 2021

Keywords:
Inconel 718
Electromagnetic ring expansion test
Laser melting powder bed fusion
Stable conduction porosity
Keyhole porosity

ABSTRACT

The paper describes Electromagnetic Ring Expansion Tests (ERET) performed on Laser Melting Powder Bed Fusion (LPBF) Inconel 718 stress relieved test pieces, to establish the effect of a randomly dispersed spherically voided microstructure on tensile ductility, fracture, and fragmentation at high strain rate ($10^{-3} < \varepsilon < 10^{4}$ s^{-1}). An empirical model to predict porosity type and growth rates as a function of laser energy density was established, to select the LPBF process parameters to fabricate test pieces under stable conduction and keyhole melting. The size, shape, distribution of macro and keyhole pores in the test pieces obtained for ERET testing were characterised. At high strain rate the number of ring fragments for the highest porosity doubled, accompanied by a reduction in true strain at maximum uniform elongation and fracture strain. The trend for reducing fracture strain with increasing porosity at high strain rate was described by a decaying power law. Overall, there was a significant positive strain rate effect on tensile ductility at lower porosities attributed strain rate hardening (Hart, 1967) [1]. Fracture surfaces containing the highest porosity identified four different void coalescence mechanisms that helped explain the influence of larger pores on the stress state in the alloy.

1. Introduction

Laser based AM (Additive Manufacturing) of nickel based alloys has seen significant interest in the repair [2,3] and fabrication [4] of high temperature components used in applications such as gas turbine engines. LPBF of nickel alloys such as Inconel 718 (IN718) for

* Corresponding authors.
E-mail addresses: p.wood7@derby.ac.uk (P. Wood), alexis.rusinek@univ-lorraine.fr (A. Rusinek), pawel.platek@wat.edu.pl (P. Platek), jacek.janiszewski@wat.edu.pl (J. Janiszewski), judyta.sienkiewicz@wat.edu.pl (J. Sienkiewicz), u.gunputh@derby.ac.uk (U.F. Gunputh), kamil.rajkowski@wat.edu.pl (K. Rajkowski), mhmiguel@ing.uc3m.es (M.H. Miguélez).

https://doi.org/10.1016/j.matdes.2021.109908
0264-1275/

precision turbomachinery components can only be considered a near net shape fabrication process that requires post-processing. This paper seeks insights into the material behaviour in a range of high speed, large strain deformation processes with damage leading to fragmentation. These include for example, foreign object damage from atmospheric dust particles, up to 100 μm diameter [5], can impact components in the turbine engine compressor. In an explosive or highspeed metal forming (HMF), the speed of the forming rates often exceeds 100 m/s with strain rates of 10^4 s^{-1} or higher. Within the group of HMF, electromagnetic forming has been used to calibrate a part shape incorporating detailed features to high precision [6], and LPBF of IN718 could be used to develop an optimum preform shape that can be finished or calibrated by HMF. Other applications are machining processes in which the chip form depends on the alloy, its microstructure and cutting speed.

1.1. Inconel 718 alloy

IN718 is a precipitation hardened nickel alloy with 3% and 9% weight fraction of γ′ and γ″ [7]. These precipitates are nanoscale [8,9] and coherent in the austenitic face centred cubic (FCC) primary γ matrix phase [10]. The δ and Laves phases precipitates are minimised to reduce embrittlement of the alloy [7] at elevated temperature. The alloy has good weldability and retains its mechanical properties at elevated temperature (650 °C) and in corrosive environments [11,12].

Sangid and co-workers [13] found the development of plastic strain in the microstructure of LPBF of IN718 in the fully hard condition was more localized than in the as-built condition regardless of build orientation with a tendency for strain localisation along 45° shear bands. The alloy therefore in the hard condition is not well suited to post fabrication processing such as machining. However due to the larger precipitates and segregation of alloying elements in the as-built LPBF IN718 microstructure, together with porosity and other defects, it may display reduced tensile ductility at high strain rate.

1.2. Laser melting powder bed Fusion (LPBF)

The LPBF uses a laser beam (either continuous or pulsed) to fully melt a thin layer of metal powder typically up to 100 μm thickness in an inert gas atmosphere. After rapid solidification, a new layer of powder is deposited, and the laser scans the deposited powder layer, melting and fusing the powder and substrate following a specific scan path. The process is repeated layer by layer until the geometry of the part is obtained. The resulting microstructure and properties of the part produced is determined by the combination of process parameters applied [14,15] and these include: laser power (P), scan velocity (V), layer height (D), hatch spacing (H), laser spot size (d), laser scanning method (raster, chessboard), powder particle size (distribution and sphericity), powder bed packing density, re-coater type and direction [16] among others. Moussaoui et al [17] identifies a convenient single measure frequently used in other works as either volume energy density (VED) or linear energy density (LED) to combine the many process parameter inputs. LED is associated with single track and single layer studies. Both measures have limitations but have been applied usefully over a specific range of power and scan velocity.

The rapid heating [18,19] of the powder layer creates a liquid melt pool with peak temperature in excess of 3×10^3 K and possibly reaching 4×10^3 K [20], that extends into the substrate and overlapping tracks. Rapid solidification with cooling rates of 10^6 to 10^8 K/s leads to a unique alloy microstructure. One example is the presence of fine cellular dendrites typically with spacing below 1 μm [21,22], a grain structure [23] of small equiaxed grains (10 μm) size at the boundary of melt pool tracks when viewed on the horizontal build plane (Parallel to build plate), and a columnar grain structure when viewed on the vertical build plane (Perpendicular to build plate).

Pore type defects that are an inherent feature of LPBF alloys have been studied to understand the conditions that promote them [14] for AlSi10Mg alloys, in a review of high temperature alloys [24]; and more recent works [25] to develop a process map for IN718 alloy by studying a wide range of process parameters to develop optimal properties with minimal defects. According to Rai et al. [26] two laser melting regimes in laser welding that can develop in LPBF depending on the energy density applied - conduction or keyhole melting. The former is associated with shallow penetration and the latter deep penetration.

1.3. Conduction mode melting

Conduction mode is a stable and desirable region for LPBF melting of alloys and with sufficient laser energy, it develops a microstructure consisting only of small pores with minimum overall relative porosity below 2% in IN718 alloy [25]. Gong et al [27] showed that reducing energy density in the conduction mode for Ti-6Al-4 V alloy below a threshold results in partial melting, which leads to balling and discontinuities in track formation. The pores that develop are irregular in shape and characterised as lack of fusion (LoF) [28] and levels of relative porosity in IN718 alloy increase rapidly to a few percent [29] and higher as energy density is further reduced. Yadroitsev et al [30] examined single tracks in IN625, 316L, H13, CuNi10, 904L alloys and proposed a simple geometry-based stability criterion to obtain a stable melt pool.

The spherically shaped pores in the alloy microstructure have been suggested to develop from entrapped gas either from the shielding gas in the powder bed or, was present in the powder during the powder fabrication process, or both [25,31–34]. Cunningham et al [32] observed spherical pores in LPBF Ti-6Al-4 V alloy typically with a pore diameters (PD) from a few microns to 19 μm under stable conduction mode melting and despite this optimum modus operandi, some small LoF pores were still visible; it was noted pore count increased rapidly with reducing pore diameter, and pores containing inert gas vapour whose buoyancy is unable to escape the melt pool quickly enough will remain in the solidified alloy [35]. The same paper also identifies porosity can be reduced or eliminated in laser welding for some alloys using a vacuum or non-inert shielding gas such as nitrogen.

1.4. Keyhole mode melting

In 2019, Martin et al [37] observed keyhole pores form along line scan paths in LPBF of Al6061 alloy at high energy density [P = 400 W, V = 800 mm/s], under an Argon environment. Keyhole melting drives excessive energy density into the powder layer and substrate with melt pool depth increasing more rapidly than its width. Because the temperature in the melt pool can reach or exceed the boiling point of the liquid alloy high vapour evaporation rates (ablation) form a vapour column. The vapour column increases absorptivity [38] which further increases the energy density delivered to the powder bed and drives the keyhole melt pool deeper into the substrate. Melt pool turbulence increases in the keyhole mode and simulations developed by previous researchers [18,19] predict a clockwise circular flow velocity between 2 and 6 m/s in the melt pool. Spatter formation and ejection also increase together with higher powder entrainment. A transition from conduction to keyhole and severe keyhole melting can be determined by the melt pool geometry [39]. When the melt pool is operating in the severe keyhole mode it is increasingly unstable with the formation of large pores at the root of the keyhole more likely.

At high energy density pores formed at the root of the keyhole in LPBF also tend to a spherical shape which has been attributed to entrapment of metal gas vapour [31,32,40]. Keyhole porosity in Ti-6Al-4 V [32] was found to be present at the border between conduction and keyhole mode melting with a maximum pore diameters PD of 36 μm; and at higher energy in the severe keyhole mode, maximum pore diameters PD increased to 133 μm. Kasperovich et al [41], in Ti-6Al-4 V, the development of large pores at excessive energy density (VED = 292 J/mm^3) with PD typically in the range 10 to 100 μm. At this high energy density, a strong correlation was observed for the distributions of pore circularity and sphericity from images obtained using a 2D optical microscope (OM) and 3D synchrotron tomography; the absolute error in relative porosity determined between the area fraction (2D) and volume fraction (3D) methods was contained to 20% at high laser energy.

1.5. Review of porosity reported in the literature for LPBF of IN718 alloy

The effect of process parameters on porosity development in LPBF IN718 alloy over a wide range of process parameters was studied by various authors [17,22,23,25,29,42,43]. Table A1 in the Appendix displays porosity measurements obtained from the literature over a wide range of energy density covering conduction melting mode at low and stable energy density, and in the keyhole melting mode. The process parameters applied vary widely for example laser power (P) range used is from 90 to 1000 W, scan speed (V) from 100 to 3000 mm/s, layer height (D) from 25 to 70 μm and hatch spacing (H) from 50 to 150 μm. Powder particle sizes ranged from 5 to 80 μm and different SLM machine systems and lasers were used. Fig. 1 displays the porosity data obtained from the literature for LPBF IN718 multilayer samples and identifies the unstable, stable conduction, and keyhole regions.

Both optical microscope (OM) and Archimedes (A) techniques were used to measure the area and volume fraction porosity respectively in the literature. Overall, the results in Fig. 1 suggest the volume energy density VED range for stable conduction melting is from 54 to 142 J/mm^3 with total volume fraction of porosity below 2%. Specific combinations of process parameters suggest porosity can be reduced to 0.5% as evidenced by the clusters of results with lower porosity. Further reduction in porosity to ~0.01% can only be achieved by Hot Isostatic Pressing HIP [17,36].

The maximum pore diameter PD identified at a VED of 167 J/mm^3 [25] in a cube shaped sample (10 × 10 × 12 mm height) was 85 μm. In the same work with VED at 169 J/mm^3 the total volumetric fraction of porosity was measured at 2.24%. The large pores fabricated at higher VED however were identified as gas entrapped pores and not keyhole porosity. At higher energy density, [23] total area fractions of porosity on the top surface of two samples were found to be at 1.05% and 6.24% with VED respectively at 220 J/mm^3 and 450 J/mm^3. With VED at 450 J/mm^3, which is in the severe keyhole regime, the authors identified them as large spherical macropores distributed over the sample surface caused by entrapped gases from vaporization within the melt pool.

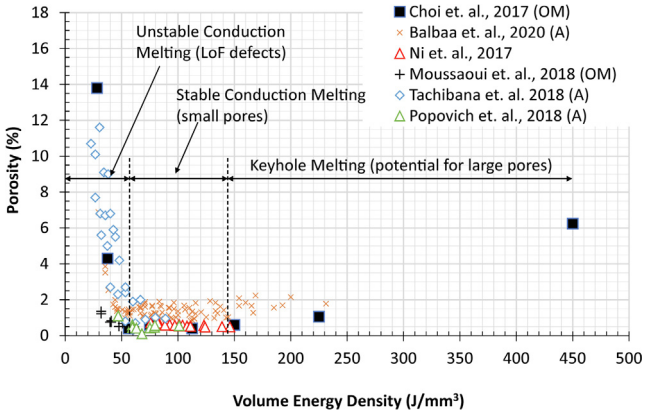

Fig. 1. Porosity measurements of LPBF IN718 samples obtained from the literature (Details in Table A1 in Appendix A) over a wide range of process parameters, machine systems and powder particle size.

1.6. Electromagnetic ring expansion test

The physics of Electromagnetic forming involves discharging electrical energy stored in high voltage capacitor banks through a coil with an event time below 100 μs. The current flows through the coil to generate a rapidly changing magnetic field, and a sudden electromagnetic force in the conductive workpiece. The electromagnetic ring expansion test [44] was developed to study tensile failure modes associated with dynamic loading and fragmentation of materials such as aluminum and copper. Furthermore, it enables obtaining a constant strain rate in comparison to the explosive loading conditions. An average strain rate in a ring sample is derived from the radial velocity of the ring divided by the radius, $\dot{\varepsilon} = \frac{V_0}{R}$. Based on [45–49] the number of fragments N will increase as the material strain hardening rate, $n = \frac{\partial \sigma}{\partial \varepsilon}$, and/or the onset of tensile instability is reduced. Instability is triggered more rapidly with localization of plastic strain. The thermal softening due to localized adiabatic heating at instability will also act to reduce hardening rate and increase N. The hardening rate acts directly on N and in a non-direct way, the effect of thermal softening due to adiabatic heating.

This paper investigates the tensile ductility and fracture with fragmentation of additively manufactured Inconel 718 (AM IN718) alloy with a voided microstructure (up to 5% volume fraction) at high strain rate ($10^{-3} < \varepsilon < 10^{4}$ s^{-1}) fabricated by LPBF. The paper seeks to understand the high strain rate effect on the limit of uniform elongation and fracture of AM IN718 in the as-built condition (with stress relief and partial anneal) fabricated at stable and higher laser energy density. The latter to develop an alloy microstructure containing randomly dispersed spherical voids. Using Fig. 1, an empirical model was developed to obtain the optimum LPBF process parameters to fabricate IN718 test pieces using selective laser melting, SLM at the University of Derby. Then to conduct high strain rate testing using an instrumented electromagnetic ring expansion test (ERET) device at Military University of Technology (MUT) and to perform micro and macro scale examination of the test pieces before and after testing.

2. Methodology

Following the development of an empirical model to predict porosity in LPBF IN718 as a function of VED, IN718 rings were fabricated and characterised with three different levels of porosity obtained in the stable conduction and keyhole melting regions. ERET testing were then performed to determine the effect of porosity on tensile ductility at high strain rate.

2.1. Empirical model to predict porosity in LPBF IN718 as a function of VED

Based on the published data in Fig. 1, a model for porosity as a function of the single process input parameter VED, covering unstable conduction, stable conduction and keyhole melting regions consists of two growth terms:

$$\Phi_{P\%}(\chi) = \alpha_1 e^{-\alpha_2 \chi} + \alpha_3 e^{\alpha_4 \chi} \quad (1)$$

$\Phi_{P\%}$ = Percentage Porosity (%); χ = VED (J/mm^3); α_i are the fitting constants whereby α_1 = 81.2; α_2 = 0.089; α_3 = 0.57; α_4 = 0.0051.

The first term is a negative growth (decay) term to describe the unstable conduction region. The second term is a growth term covering the initial slow growth in porosity in the stable conduction region and then more accelerated growth progressing into the keyhole region. The equation (1) best fit to the published data taken from Fig. 1 is displayed in Fig. 2, with relative measure of fit (R^2 = 0.8) and absolute measure of fit RMSE = 1.08%. The coefficient α_1 is the intercept on the ordinate axis and can be readily observed if plotted on a logarithmic scale (Figure (2b)) and it should not exceed the value 100. The coefficient α_3 is also the intercept on the ordinate axis. The coefficients α_2 and α_4 are respectively the decay and growth rate terms, which are linear slope terms on a logarithmic ordinate scale. The values of the coefficients can be adjusted to calibrate the porosity equation (1) to a specific range of interest. For example, at the turning point between decay and growth terms, the minimum porosity (VED = 77 J/mm^3) can be made sharper and shifted either to the left or right along the abscissa axis.

Equation (1) describes the trend for porosity over the unstable, stable and keyhole regimes as a function of the single process input parameter VED. The rate of porosity increase, in the unstable conduction region, is sensitive to small reductions in VED. On the other hand, the transition into the keyhole region from the stable region is less sensitive suggesting porosity levels can be controlled or graded by process design. The model of porosity versus VED for LPBF IN718 enables selection of the process parameters in the stable conduction and keyhole regimes suited to the machine type in this study.

2.2. Experimental methods - preparation of LPBF IN718 samples

Three tube sample groups were produced in IN718 alloy in the same build, each with different process parameters using a Renishaw AM250 Selective Laser Melting machine. This type of machine incorporates a fibre laser with pulse-modulation (movefire); so that scan velocity is determined by the point distance on the same line scan path divided by the time of exposure. A soft re-coater using a cylindrical silicone strip mounted in the wiper housing was used with motion from the back to front of build plate. The IN718 powder material supplied by Renishaw was spherical, with particle diameter size between 15 and 45 μm, and chemical composition displayed in Table 1. Each tube with nominal dimensions measuring (mm) 34.4 outer diameter, 1 wall thickness and 50 height was printed on the same build plate with the major axis of each tube aligned to the vertical orientation (Z). The horizontal build plane (XY) is normal to the vertical build axis Z. The VED used for volume fill for tube samples T1, T2 and T3 was respectively = 74.1 J/mm^3, 139 J/mm^3 and 167 J/mm^3. Meander scanning was used for each layer and the beam compensation was set to 60 μm. With each layer, the volume (or fill) is scanned first, followed by the boundaries (outer and inner border) and the laser spot scans each layer at an angle of 67° with respect to the previous one [50,51]. Common process parameters applied to each tube sample (μm) were D = 30, H = 90, and spot size 70. The build orientation and corresponding process parameters are displayed in Fig. 3 and Table 2.

The argon purge pressure in the build chamber maintained an atmosphere with oxygen content <1000 ppm (0.1%) in accordance with powder supplier (Renishaw) [52]. After finishing the build process, the tubes were stress relieved whilst still attached to the build plate at 982 °C for 1 h followed by a slow furnace cool. It is to be noted that the AM tube samples were neither subjected to Hot Isostatic Pressing HIP nor to strength hardening heat treatments.

Inductively Coupled Plasma and Optical Emission Spectrometry (ICP-OES) was used to confirm the chemical composition of a printed cube sample using the same process parameters for tube sample T1. The results of the chemical analysis are displayed in Table 1 and confirm the specifications of the alloy are in accord with standards.

2.3. Porosity measurements in rings

Macroscopic measurement of porosity was performed using a Keyence VHX6000 digital light microscope (OM). For the porosity measurements, three tube ring samples from each tube group were sectioned, mounted in epoxy resin with the tube top plane exposed for analysis. They were then metallographically ground and finish polished using an aqueous solution of silica. For the measurement of pore diameter (PD) above 3 μm, a Keyence Z1000UR lens was used at a magnification of 500x giving a resolution of 0.43 μm/pix. The image region covered to measure porosity was approximately 5 mm^2 for each ring sample giving a total of nine images. In all cases PA below 10 μm^2 (PD < 3 μm) was filtered and removed due to noise. A Phenom ProX/CeB6 scanning electron microscope (SEM) with an acceleration voltage at 15 kV, equipped with an energy dispersive spectroscopy (EDS) chemical composition analyser, was used to examine the smaller pores on a region approximately 0.032 mm^2. Using both OM and SEM, fracture surface examination was carried out after the electromagnetic ring expansion testing and cleaning in acetone.

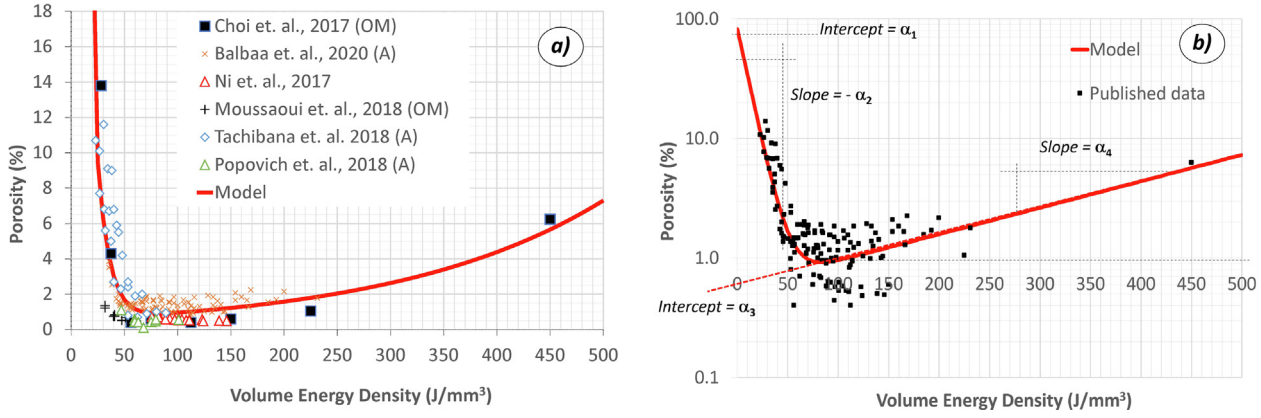

Fig. 2. Best model fit to published data of relative porosity and VED in LPBF of IN718 (a) and same model and porosity data on a log ordinate scale (b).

Table 1
Composition of the IN718 powder and small printed cube using T1 process parameters (in percent weight).

Elements (w%)	Ni	Cr	Fe	Nb + Ta	Mo	Ti	Al	Co	C
IN718-0405 Powder (Renishaw)	50.00–55.00	17.00–21.00	Balance	4.75–5.50	2.80–3.30	0.65–1.15	0.20–0.80	<1.00	0.02–0.05
Chemical Analysis of Sample Cube	53.7	18.4	18	5.13	3.08	0.95	0.47	0.09	0.053

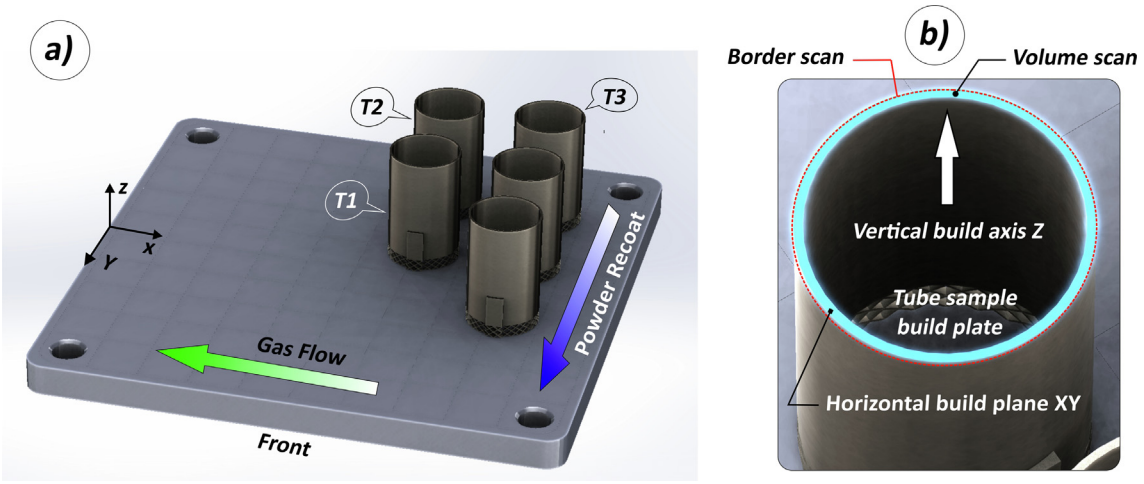

Fig. 3. Additive manufacturing (AM) of tube samples, T1, T2 and T3, using the Renishaw AM250 SLM machine (a) and tube sample build orientation definitions (b).

Table 2
AM processing parameters used for the fabrication of tube samples T1, T2, and T3.

LPBF Tube ID	Units	T1		T2		T3	
		Fill	Border	Fill	Border	Fill	Border
Laser power	W	200		175		175	
Exposure time	μs	70	50	150	150	180	180
Point distance	μm	70	20	70	20	70	20
Scan speed	mm/s	1000	400	467	133	389	111
Energy density	J/mm^3	74.1	185	139	486	167	583

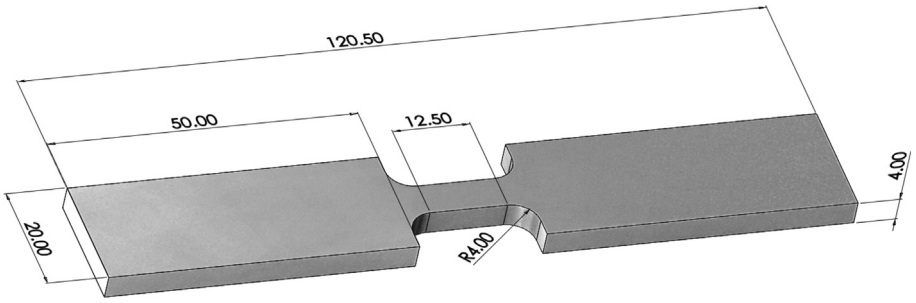

Fig. 4. Geometry of uniaxial tensile test piece.

2.4. Microhardness measurement

Microhardness testing was carried out on the build axis of each tube T1, T4 and T5 using the Micro Vickers hardness tester and method Hv0.2. The latter test was done at 10 positions equally spaced at typically 1.2 mm pitch between indents.

2.5. Uniaxial tensile testing

LPBF IN718 samples for uniaxial tension testing in the horizontal and vertical orientations, with the geometry displayed in Fig. 4, were fabricated (4 in each direction) using the T1 tube sample process parameters and the same chamber environment. Samples for uniaxial testing were stress relieved whilst on the build plate, then wire cut and were not machined to finish. Tensile testing was performed using an electromechanical Shimadzu AG-X test machine with 100kN load cell and Epsilon extensometer model 3542, in accord with ASTM E8/E8m-13a. Mechanical properties measured were yield strength, tensile strength, elongation at fracture and reduction of area of fracture surface.

2.6. Electromagnetic ring expansion test (ERET)

The electromagnetic ring expansion (ERET) test set up at the Military University of Technology (MUT) in Warsaw displayed in Fig. 5 is based on the construction by Grady and Benson (1983)

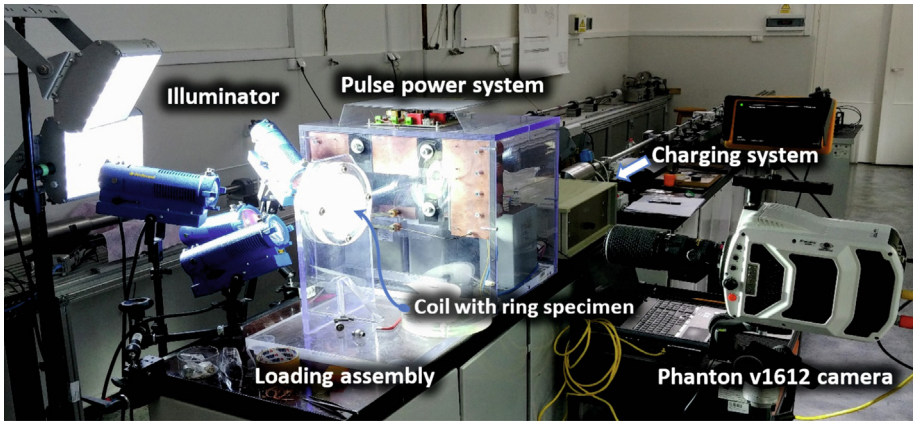

Fig. 5. View of the MUT arrangement for electromagnetic ring expansion testing.

and Gourdin (1989) [45,53]. The ERET equipment consists of three main components: A pulse power system with 240 μF capacitor bank and two impulse thyristors, a loading assembly and charging system. The coil consists of six turns of 1.2 mm diameter oxygen free high purity copper wire wound without pitch on a polyacrylic mandrel, to which each ring sample was attached for testing. Coil turns were potted in epoxy resin which was reinforced with a glass fibre filler. The loading assembly consists of two 20 mm polycarbonate plates with cavities, to support the coil with ring sample attached. A wax ring is fitted to the outside of the cavity to capture fragments generated during fracture of the ring sample. A full description of the ERET equipment used in the present work is given by Janiszewski and Pichola (2009) [48] and Janiszewski (2012) [49].

The tube samples were cut from the build plate using wire electrical discharge machining (wire cut). Each tube was precision turned on the outer and inner diameters (approximately 0.3 mm removed) to the tolerances required, and then EDM wire cut to create individual ring samples as displayed in Fig. 6, each with nominal dimensions (mm) 33.6 outer diameter, 0.7 wall thickness (t) and 1 height (z), providing 10 ring samples per tube group (Fig. 6 (a)).

A high purity copper driver ring [47] displayed in Fig. 5b was used in the ERET to minimise the heat transfer to the IN718 ring sample developed by the high current discharge. Machining tolerances for the copper driver ring with dimensions (mm) 0.5 thick, 3 wide and inside diameter 31.2 provided a slight interference fit between the IN718 ring sample and driver ring Fig. 6(c).

Discharge voltages from the capacitor bank were applied in the range 2500–2900 V with the latter required to fragment each IN718 ring sample as displayed in the Fig. 7. The applied discharging voltage from the capacitor bank was extremely high and frequently resulted in coil damage and replacement after a few tests. It was noted coil damage also occurred if the tested ring position was not correctly adjusted to the driver ring or the coil, then the test ring slid often off the driver ring during the test, which resulted in disturbance of the expansion process and generation of very large forces on the coil turns. Results from failed tests were discarded. Five successful ERET test results were each obtained for T1 and T2 ring samples and three ERET test results for T3 ring samples.

Ring displacement with time during the test was recorded with a Phantom v1612 high speed camera. For maximum accuracy, the observation field was selected in which only a moving ring segment and two calibration target markers were recorded (distance between markers was 5 mm) with optical resolution of 256 × 32 pixels. Each image was recorded at a time interval of 1.6 μs (626,900 frames per second). TEMA software (Imagesystems, Sweden) suite for advanced Motion Analysis tests, was used to derive the ring expansion velocity versus time history from the high-speed video images.

The strain rate is derived from the ring expansion velocity $(V_0(t))$ and the current radius (r) as follows:

$$\dot{\varepsilon}(t) = \frac{V_0(t)}{r} \tag{2}$$

Strain at maximum uniform elongation in ring fragments was measured before the start of necking strain:

$$\varepsilon_u = \ln\left(\frac{A_i}{Au}\right) \tag{3}$$

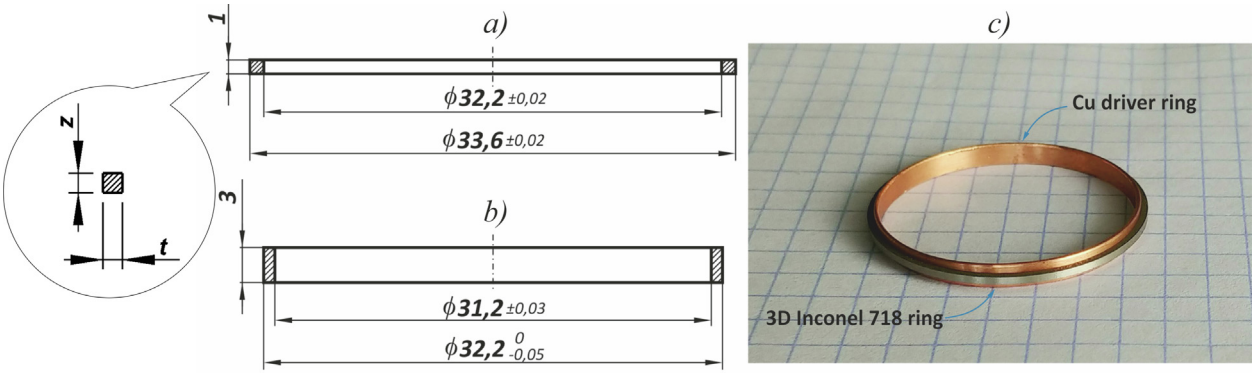

Fig. 6. Dimensions of Cu driver ring (a) and assembly of IN718 and Cu driver ring (b) mounted ring samples (c).

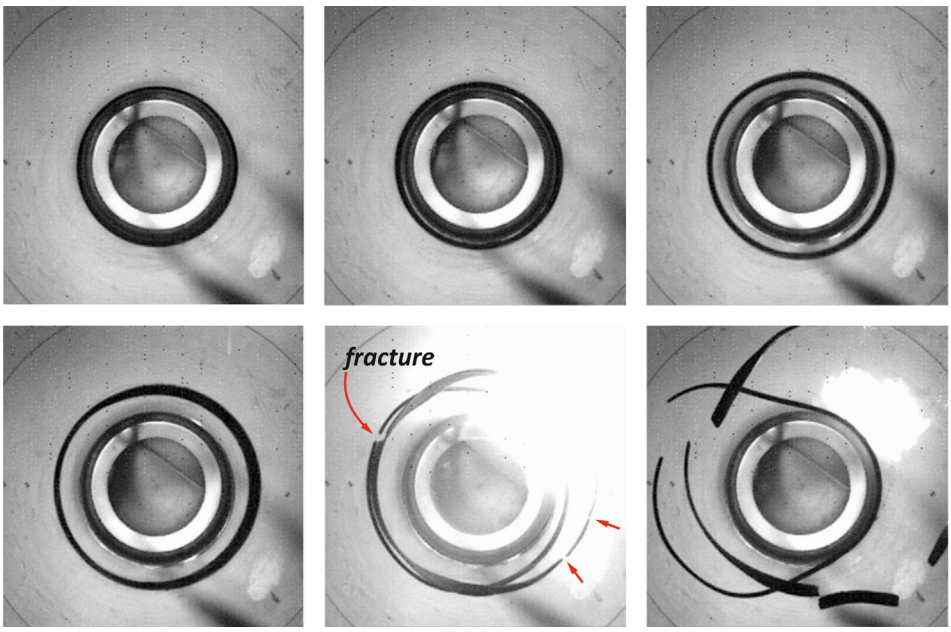

Fig. 7. Ring expansion with fracture using capacitor discharge voltage of 2900 V (resolution is 256 × 256 pixels with 4 μs time intervals between frames using a frame rate of 66,000 frames per second).

where A_i and A_u are the initial and the deformed cross-sectional areas, respectively.

A_u was determined from measurements of the cross-section dimensions of recovered ring fragments using a blade micrometer with a non-rotating spindle and precision to ±5 μm). Dimension of the A_u was determined in the middle of the ring fragment or between neighbouring arrested necks which is assumed to be a suitable indicator of maximum uniform strain and the initiation of localization or necking.

Based on elongation, the strain at fracture is derived as follows:

$$\varepsilon_{lf} = \ln\left(\frac{r_f}{r_i}\right) \tag{4}$$

where r_i and r_f are the initial and the deformed lengths.

r_f was measured from the length of each fragment captured in the wax ring using a Keyence VHX6000 digital microscope.

3. Results and discussion

For convenience it is useful to distinguish macro and micro porosity in this paper. The definition of a macro pore in the context of LPBF is a defect typically visible to the naked eye, but to measure its characteristics requires an OM at 500x magnification. The definition of a micro pore is a defect that cannot practically be observed without an OM at higher magnification and measurement of its characteristics requires an SEM.

3.1. Macro porosity

Fig. 8 displays images of porosity for T1, T2 and T3 rings on the horizontal build plane. For the T1 ring sample there are very few macro pores and six are identified by the arrows. The porosity increases in the T2 ring sample with maximum porosity in the T3 ring sample. The shape of the pores on the horizontal build plane of each ring is circular. Three rings obtained for each tube group T1, T2 and T3 were selected to characterise the macro porosity using OM and the results displayed in Table 3. The image area for measurement of porosity was in the range from 4.1 to 5.8 mm^2.

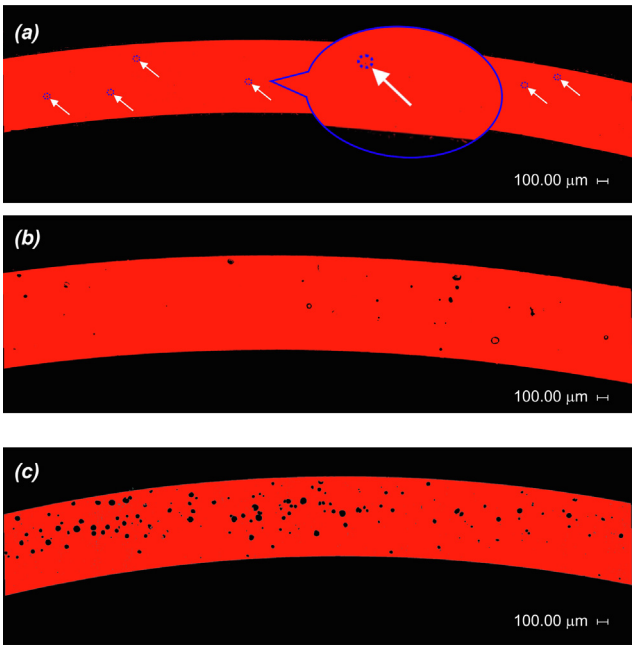

Fig. 8. Image of macro pores on horizontal build plane of T1 ring sample (a), T2 ring sample (b), and T3 ring sample (c).

Fig. 9 displays the macro porosity histograms of three rings obtained for each tube group. The scale for the PA bin is logarithmic while PD is identified within brackets. The porosity distribution for the T1 rings is normal. The lower limit of resolution to measure macro pores using OM at 500x magnification on an image area ~5 mm^2 was a PD > 1 μm. The modal PD for each T1 ring is 6.3 μm and the area fraction occupied is 0.04%. The average total area fraction of porosity for the T1 rings was 0.1%. Gribbin et al [51] using high resolution μXCT scan imaging determined the volume fraction of porosity in LPBF IN718 at 0.18%; the test pieces were fabricated with VED at 74 J/mm^3 which is the same energy

Table 3
Characterisation of macro pore size, shape and distributions for rings obtained from T1, T2 and T3 tubes.

Tube ID and ring sample ID	Image area for porosity measurement mm^2	Shape of distribution (PA on log10 scale)	No of PA bins containing data	Pore shape on top plane	Modal PD µm	Max PD µm	Total area fraction of porosity %	Average area fraction of porosity %
T1-S1	5.0	Normal	5	circular	6.3	25	0.07	0.1
T1-S2	4.6		5	circular	6.3	19	0.10	
T1-S3	4.1		5	circular	6.3	11	0.09	
T2-S1	4.2	Normal	7	circular	20	67	0.49	0.3
T2-S2	4.1		7	circular	20	51	0.14	
T2-S3	4.4		7	circular	11	56	0.28	
T3-S1	5.8	Strong negative skew	7	circular	63	87	3.29	3.4
T3-S2	5.6		7	circular	63	93	4.01	
T3-S3	4.9		7	circular	63	81	2.98	

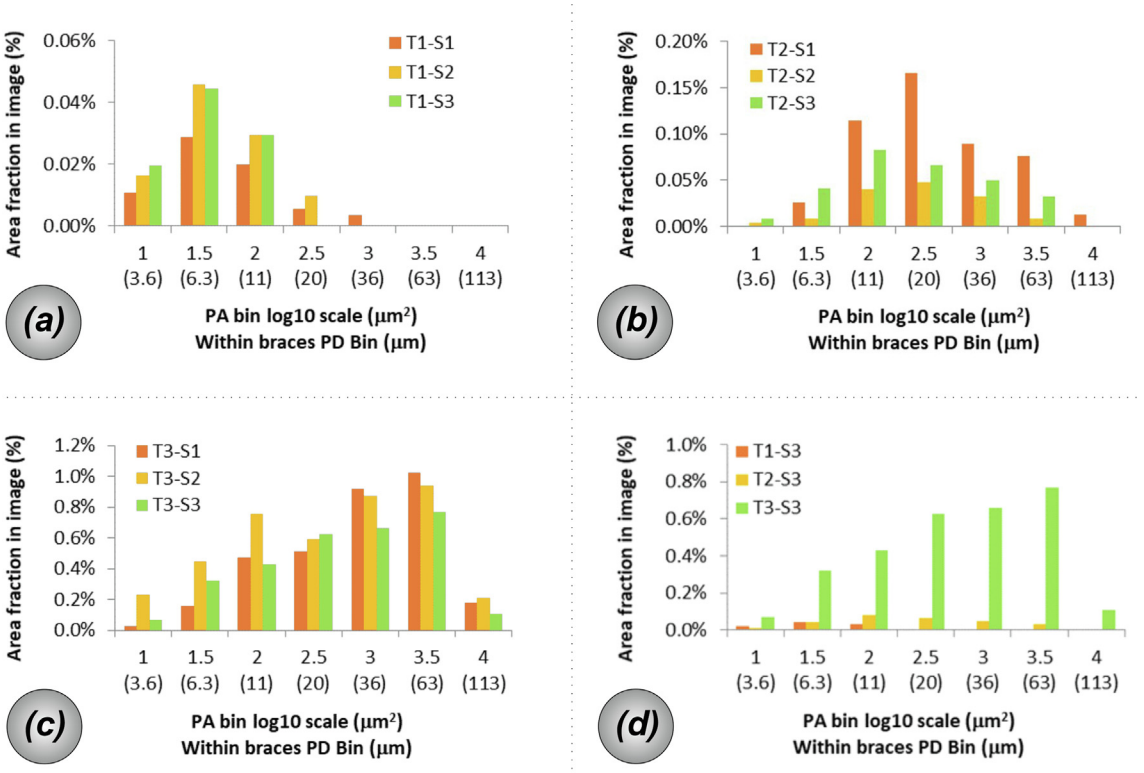

Fig. 9. Porosity distributions on horizontal build plane of tube rings: T1 (a), T2 (b), T3 (c), and sample (S3) rings from T1, T2 and T3 tubes (d).

density used to fabricate the T1 tubes in this paper, although a different combination of P, V, H and D parameters were used (Table A1 in Appendix).

Porosity distributions for the T2 and T3 rings displayed in Fig. 8 occupy the full 7 bins assigned. The distributions for the T2 rings are normal and T3 rings display a strong negative skew. The modal PD respectively for the T2 and T3 rings was 20 and 63 µm and the corresponding area fraction of porosity for the modal PD did not exceed 0.16% and 1%. For the T2 and T3 rings the average total area fraction of porosity was 0.3 and 3.4%. The measured maximum PD in the T1, T2 and T3 rings was respectively 25, 67 and 93 µm. However, the distributions for T2 and T3 rings in Fig. 9 identify the likelihood of a slightly larger maximum PD of 113 µm; but this only occupies a small area fraction of porosity in the right-hand tail of their corresponding distributions respectively below 0.01 and 0.2%. It is noted the maximum PD for the T3 rings at 93 µm occupies 13% of the ring wall thickness (700 µm). The Fig. 8 lower right compares the porosity distributions of a T1, T2 and T3 rings on one histogram so the relative scale effect can be visualised. The level of macro porosity in the T1 and T2 rings associated with the VED range between 73.1 and 139 J/mm^3 is very low, because this processing window promotes the formation of smaller spherical pores under stable conduction mode melting [32,34].

The negative skew for the distribution of macro pores in the T3 rings developed at higher energy density with VED at 167 J/mm^3 (P = 175 W, V = 389 mm/s, H = 90 µm, D = 30 µm) suggests a tendency for the unstable melt pool to form larger spherical pores. In 2020, Balbaa et al [25] measured relative porosity in LPBF IN718 at the border between keyhole and severe keyhole regimes at 2.24% with VED at 169 J/mm^3 (P = 270 W, V = 500 mm/s, H = 80 µm, D = 40 µm) which is very close to the VED applied in this study. Although a slightly higher average overall porosity of 3.4% was obtained in this study. The distributions obtained for T2 and T3 suggest a PD of 113 µm is a maximum, and further increases in VED would only serve to increase the number of larger pores but not their size.

3.2. Micro porosity

SEM images of rings at 1500x magnification taken on the horizontal build plane with image region 0.032 mm^2 display micro porosity in Fig. 10. Micro pores were circular in shape for the T1, T2 and T3 rings. Each micro pore identified by an arrow with the corresponding pore diameter is between 1 and 9 μm. Micro pores between 2.6 and 4.8 μm were observed [51] in LPBF IN718 test pieces fabricated with VED at 74 J/mm^3, which is the same energy density used to fabricate the T1 tubes in this paper and consistent with those identified in T1 ring displayed in Fig. 10(a). The total area fraction of micro porosity (PD < 5 μm) however did not exceed 0.2% in all rings examined.

Elmer et al [35] identified a bimodal distribution of porosity in keyhole laser welds with large pores being formed at the root of the keyhole and smaller pores at the top of the weld. In the same way for LPBF, apart from the entrapped gas that may have already been present in the powder during its fabrication, small spherical pores could also form near the top of the melt pool under stable conduction and unstable keyhole melting regimes. In keyhole melting, larger spherical pores formed at the root of the keyhole would eventually coexist with smaller pores on the same horizontal build plane due to the building up of layers.

In the keyhole melting region the melt pool penetrates the substrate to significant depth although keyhole porosity may not develop. For keyhole melting the melt pool depth (z) to half width (d/2) is greater than 1 [39] and for severe keyhole melting greater than 2.5. On the assumption d equals the hatch spacing (90 μm), the depth of melt pool penetration z is 45 and 113 μm respectively for keyhole and severe keyhole melting. The melt pool depth z includes the powder layer thickness (in this study D = 30 μm). Assuming a powder-bed compaction density of 55% for nickel based alloy [16], under severe keyhole melting the melt pool penetrates 97 μm into the substrate. The modal PD for the T3 ring samples was 63 μm and the largest measured PD was 93 μm, suggesting the process was operating under severe keyhole melting. In single track studies of LPBF IN718 in the keyhole regime Balbaa et al [25] measured melt pool depth z at typically 100 μm with P at 170 W.

The skin produced by the exterior and interior border scan at higher laser energy density which can be a source of porosity, was machined off (150 μμm per side) to correctly size the rings at 0.7 mm thickness. Therefore macro pores formed by laser deceleration at end of track turning points [37] would have been removed.

Based on the published works of Kasperovich et al [41] and others, all circular shaped micro and macro pores are assumed to be fully spherical with error contained to 20%. Therefore, the measured area fraction of porosity on the horizontal build plane is equal to the volume fraction.

3.3. LPBF IN718 alloy mechanical properties and microstructure

Microhardness results on the tube horizontal build plane are displayed in Fig. 11. The slight sinking of the sides between the major diagonals is attributed to the softened state of the alloy. The range of the major diagonal indents for 10 microhardness readings in each ring sample was between 30 and 36 μm with an average hardness ($Hv_{0.2}$) respectively for T1, T2 and T3 at 299, 314 and 293. These results are consistent with the findings of Choi et al (2017) and Moussaoui et al (2018) [17,23] in the stable VED range for as-built samples; the former reporting an average microhardness of 312 $Hv_{0.5}$ and the latter between 310 and 334 HV. The findings of Choi et al [23] identified increasing variability at higher energy density typically in the keyhole regime and a reduction from 312 to 290 $Hv_{0.5}$, which is consistent with the findings in this paper as displayed in Fig. 11(b). The lower value of 80.5 $Hv_{0.2}$ for the T3 ring sample may be attributed to a subsurface macro pore in the vicinity of the indent and the higher hardness of 410 $Hv_{0.2}$ to a hard phase in the microstructure although the higher hardness was not observed by Choi et al.

A quasi-static engineering stress versus strain curve obtained for a horizontal (XY) and vertical (ZY) test piece at room temperature is displayed in Fig. 12. The LPBF IN718 alloy in XY and ZY were fabricated using the T1 tube sample process parameters and the properties are in accordance with the powder supplier's data sheet [52].

The anisotropic tensile properties of as-built XY and ZY test pieces have been widely reported [13,21,28,43,54] with XY displaying higher strength and lower ductility than ZY. Anisotropy being attributed to a long columnar grain structure in the vertical build axis direction (ZY) and a more equiaxed grain structure on the horizontal build plane (XY) [23,43]. The horizontal build plane (XY) is orientated to the circumferential and radial axes of the tube rings. The quasi-static mechanical properties of XY test pieces are given in Table 4. The results are in accordance with the powder supplier's technical specification for the IN718 alloy for as built

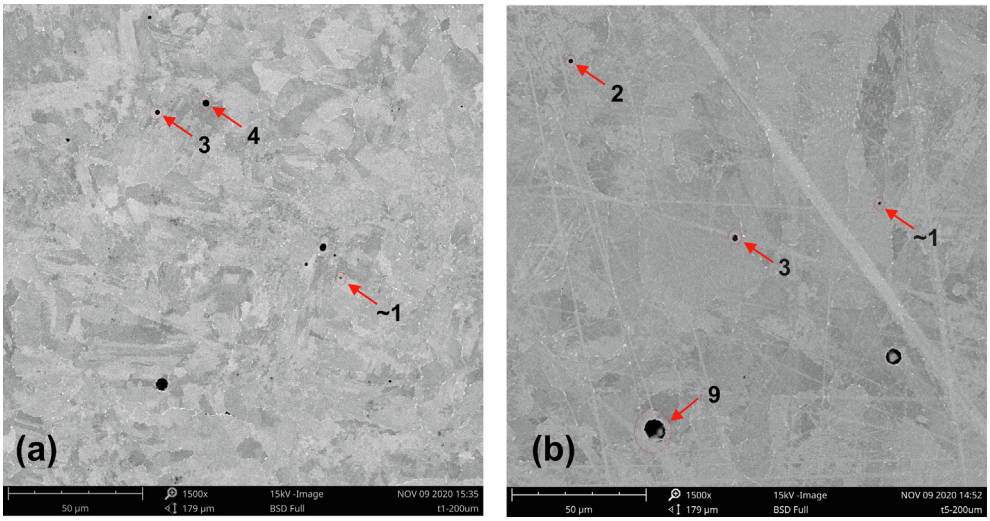

Fig. 10. SEM images of micro porosity on the horizontal build plane: T1 ring sample at 1500x mag (a), and T3 ring sample (b).

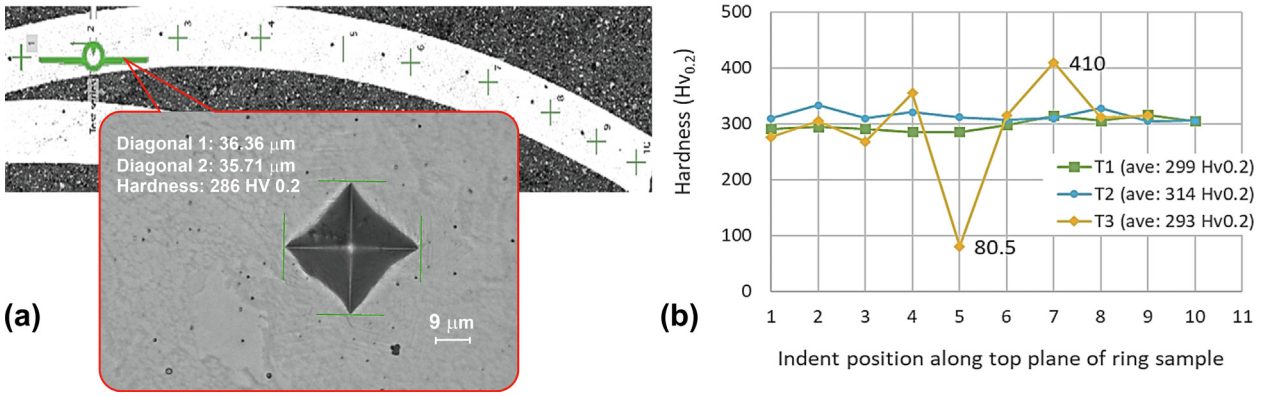

Fig. 11. Typical micro hardness indent (a) and microhardness test results (b).

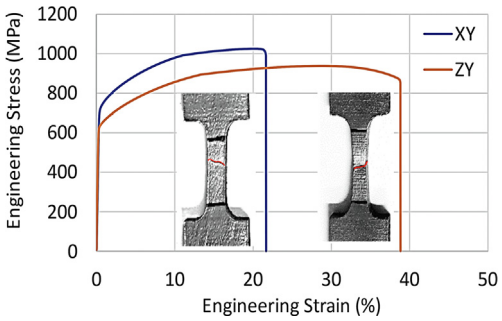

Fig. 12. Engineering stress versus strain curves of LPBF IN718 alloy fabricated in XY and ZY and samples displaying the fracture profile on gauge length.

with stress relief and 30 μm layering. The limit of uniform elongation (ε_u) for XY is 0.18 and the difference between ε_{Lf} and ε_u confirms little necking beyond tensile strength (0.02). Whilst for ZY, the difference between ε_{Lf} and ε_u respectively, 0.38 and 0.31 is 0.07, confirming significantly more localisation before fracture than XY as displayed in Fig. 11.

Small equiaxed grains of 10 μm diameter on the horizontal build plane of T1 and T3 ring samples in Fig. 13 identified by 'a', are surrounded in some cases by larger grains. Small equiaxed grains of 10 μm average size were observed by Choi et al. [23] and 30 μm by Mostafa et al (2017) [55] at the edges of scan tracks which formed by partial remelting of a neighbouring track. The test pieces studied by Choi et al [23] were cube shape of 1 cm side length. The small grain size was attributed to the rapid cooling rate of the melt pool at overlapping track boundaries, whilst grain size between tracks can typically extend over the hatch distance. Needle and plate shaped second phase precipitates are visible at grain boundaries of the T1 and T3 rings in Fig. 13 up to 2 μm in length.

EDS analysis on a region suggests element concentrations are rich in Nb, Ti, Al and Mo with relative weight of Nb respectively for T1 and T3 rings at 7.77 and 7.51%. Concentrations of Ti are higher for T3 (2.09%) as compared to T1 (1.08%). Spot analysis on the precipitates suggests a higher Nb content in T3 rings which promotes Laves and δ-phase that serve to embrittle the alloy. Within grains, precipitates (~1 μm) are also visible suggesting micro segregation of Nb [54] in the primary γ phase and is typical of rapid cooling associated with LPBF. Homogenisation, solution anneal, and age hardening will result in the precipitates being dissolved in solid solution and reformed as finely dispersed γ' and γ" phases with Laves and δ-phase minimised. HIP will reduce porosity in the alloy.

3.4. ERET ring expansion velocity and strain rate

The ring expansion velocity results obtained for T1, T2 and T3 tested rings are displayed in Fig. 14 and all results display a similar profile, with a near constant acceleration to peak velocity before decelerating to fracture. The event time occurs in under 60 μs, and the results obtained for the peak ring expansion velocity for all tested ring samples are between 140 and 157 m/s displaying remarkably high precision falling within a spread of 8%. Ring fracture occurred at expansion velocities between 30 and 60 m/s. The end of each velocity curve is not the fragmentation velocity, but the time of appearance of the electric arc which blinds the camera sensor. Instead, the velocity at fragmentation was determined to higher accuracy from the ring radius (r_f) at fracture and a linear approximation of the velocity versus time curve in the deceleration phase just after peak velocity, typically from 28 μs.

Using equation (2), the tensile strain rate at peak expansion velocity and at fracture for all tested rings is displayed in Fig. 15 and the average values given in the table (Table 5). The average strain rate $\dot{\varepsilon}_{ave}$ at peak expansion velocity is between 7.58×10^3 to 7.92×10^3 s^{-1}, the latter suggesting no significant difference. Whilst $\dot{\varepsilon}_{ave}$ at fracture is between 1.47×10^3 and $3.05\ 10^3$ s^{-1}. Fracture occurring at higher $\dot{\varepsilon}_{ave}$ for all T3 rings.

Table 4
Room temperature static tensile properties of LPBF IN718 alloy fabricated in XY.

Sample ID	Yield strength $\sigma_{0.2}$	Tensile strength σ_{UTS}	Modulus E	True strain at tensile strength ε_u	Linear fracture strain (elongation) e_{Lf}	Logarithmic fracture strain (elongation) ε_{Lf}	Logarithmic fracture strain (reduction of area) ε_{Af}
	MPa	MPa	GPa	mm/mm	mm/mm	mm/mm	mm^2/mm^2
XY1	748	1033	–	0.16	0.19	0.17	0.35
XY2	759	1044	213	0.20	0.23	0.21	0.34
XY3	717	1024	212	0.20	0.23	0.21	0.36
XY4	727	1025	223	0.18	0.22	0.20	0.36
Average	738	1032	216	0.18	0.22	0.20	0.35
Standard deviation	19	9	23	0.02	0.02	0.02	0.01

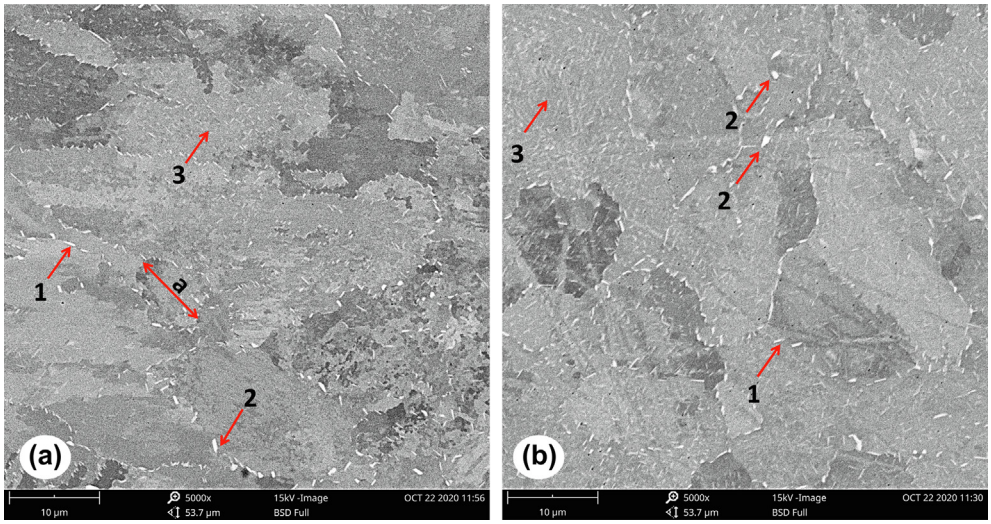

Fig. 13. Microstructure of the rings on the horizontal build plane T1 (a) and T3 (b) with second phase precipitates (1) needle and (2) plate shaped at grain boundaries ~2 µm and (3) dispersed within grain ≤ 1 µm.

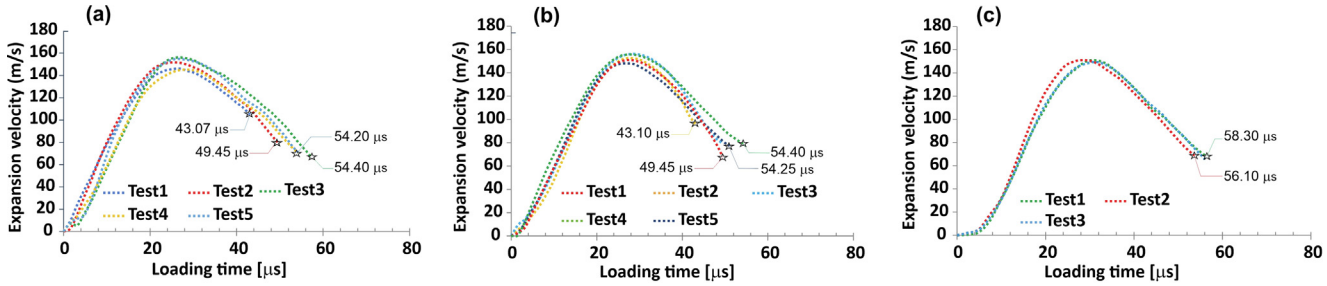

Fig. 14. Expansion velocity curves for T1 (a), T2 (b) and T3 (c) ring samples.

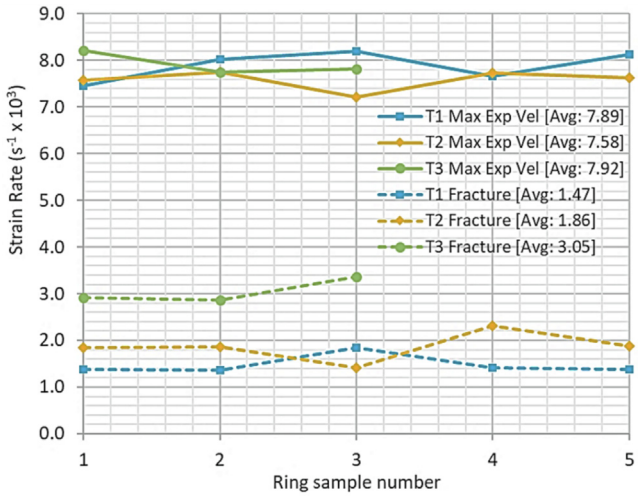

Fig. 15. Strain rate at peak expansion velocity and fracture for T1, T2 and T3 rings.

Fig. 16 displays the reassembled T1, T2 and T3 ring fragments and the average number of fragments (N) obtained for the ring samples tested. In the centre of each image is an undeformed ring. The N for T1 and T2 rings was between 2 and 4 with average 3, whilst N for T3 ring was 8 for all rings tested in this group.

3.5. Tensile ductility

The limit of true uniform elongation ε_u for the T1, T2 and T3 rings derived using equation (3) is given in Table 5. The measurement of ε_u was not precise due to slight distortion along the length of each ring fragment and measurement error could be up to 2%. Nevertheless, the trend at high strain rate is a reduced ductility with increased spherical porosity with ε_u for T1 and T3 respectively at 0.25 and 0.21. The ε_u obtained for the XY quasi-static test pieces (Table 4) fabricated using the T1 LPBF process parameters was 0.18, which is significantly lower than the T1 ring at high average strain rate ($\dot{\varepsilon}_{ave}$ = 7.89 × 10^3 s^{-1}). The higher ductility is attributed to strain rate hardening in the alloy [1] which delayed the onset of localisation under uniaxial tension. The marginally higher value of ε_u obtained for T2 over T1 may be attributed to a systematic measurement error.

The fracture strain ε_{Lf} derived from equation (4) for the T1, T2 and T3 rings are given in Table 5. The ε_{Lf} is derived by reassembling the ring fragments captured in the wax ring and measuring their length using a Keyence VHX6000 digital microscope. The ε_{Lf} is a measure of the relative elongation of a ring sample at fracture and using this method the maximum measurement error is below 0.25%. The ε_{Lf} results display high consistency within each group with average values for T1 = 0.29, T2 = 0.27 and T3 = 0.24. The ε_{Lf} for the three groups of results display significant ductility. The highest tensile ductility for T1 rings and lowest for T3 rings.

Fig. 17 displays fracture surfaces of T1, T2 and T3 ring fragments at low magnification alongside a static tensile tested XY sample number 3 (Table 4) that was fabricated using the T1 LPBF process parameters. The shape of the XY3 fracture surface Fig. 17(a) retains high shape regularity whilst all ring fragments exhibit distortion. The latter may be attributed to the dynamic stress state with unloading at multiple neck points at the start of localisation; practically this effect would distort the shape of the deforming ring and

Table 5
True strain at maximum uniform elongation using equation (3), and fracture strain using equation (4) for T1, T2 and T3 rings.

	Ring sample ID					
	T1		T2		T3	
	ε_u	ε_{Lf}	ε_u	ε_{Lf}	ε_u	ε_{Lf}
Test 1	0.25	0.28	0.27	0.28	0.21	0.23
Test 2	0.26	0.30	0.27	0.27	0.22	0.24
Test 3	0.25	0.28	0.26	0.26	0.21	0.24
Test 4	0.25	0.29	0.26	0.27	–	–
Test 5	0.25	0.28	0.25	0.26	–	–
Average	0.25	0.29	0.26	0.27	0.21	0.24
Standard Deviation (x100)	–	0.66	–	0.73	–	0.50

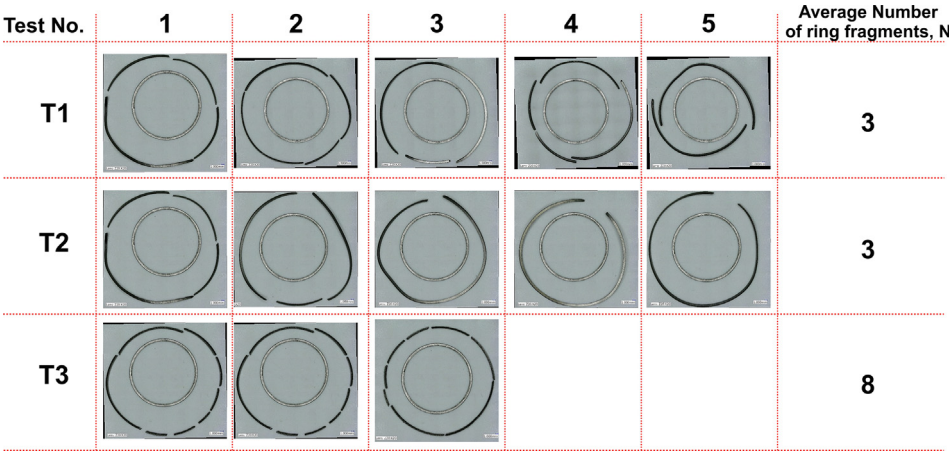

Fig. 16. Reassembled T1, T2, T3 ring fragments and the average number of fragments associated.

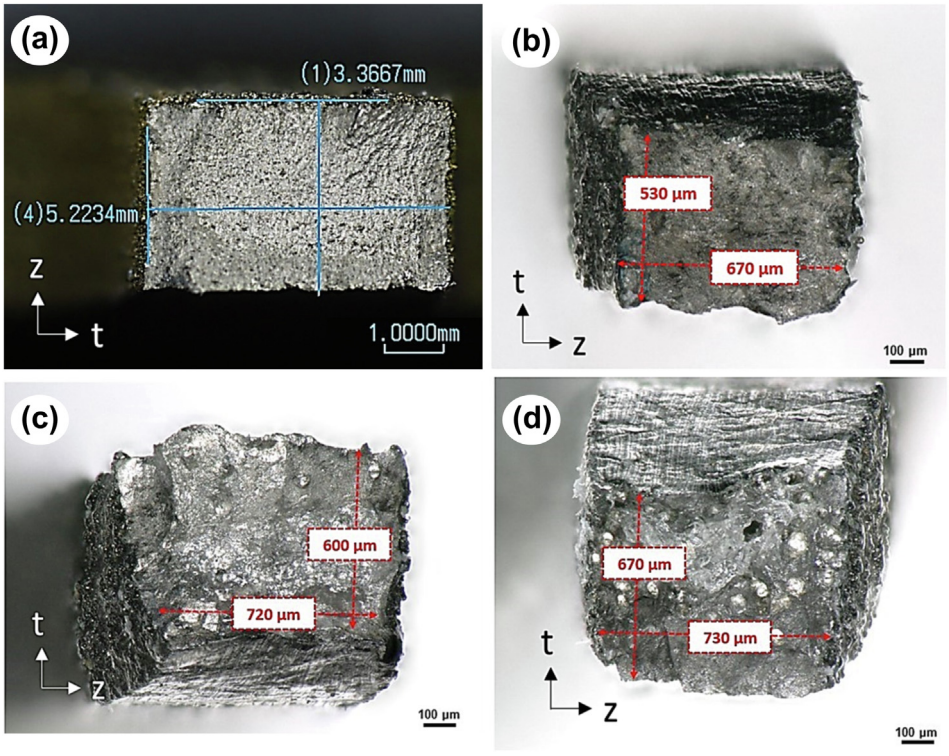

Fig. 17. Fracture surfaces at low magnification: XY3 static tensile test piece (a), T1 ring fragment (b), T2 ring fragment (c), and T3 ring fragment (d).

the reassembled ring fragments in Fig. 16 verify this. Table 6 displays fracture surface measurements obtained from Fig. 17. The measured fracture strain, ε_{Af}, enables a direct comparison of tensile ductility associated with necking strain at low and high strain rate because it is not dependent on the gauge length of a test piece. Comparing ε_{Af} for XY3 (0.35) and T1 (0.68) the tensile ductility of the LPBF IN718 alloy at high strain rate (1.47×10^3 s^{-1}) is significantly enhanced. Whilst ε_{Af} for the T3 ring (0.36) displays considerably lower tensile ductility by this measure and comparable to the XY3 sample tested at quasi-static strain rate (~10^{-3} s^{-1}).

In Table 6, fracture strain in the vertical build axis direction (ε_{zf}) for T1, T2 and T3 ring fragments was higher than the fracture strain in the horizontal build plane (ε_{tf}) for T1, T2 and T3 ring fragments.

Noting t is the difference between ring outer and inner ring radius. Similar observations were made for XY3 whereby ε_{zf} was also larger than ε_{tf}. The fracture strain ratio $R_f = \varepsilon_{zf}/\varepsilon_{tf}$ exemplifies the anisotropy in material behaviour with XY3 and T1 displaying the same R_f value of 1.4. Although the R_f value increased for T2 and T3 respectively at 2.1 and 7.2. The LPBF IN718 alloy in Fig. 12 displays anisotropic behaviour associated with build orientation. Comparing XY with ZY results, the former exhibiting higher hardening rate and higher strength in the ring t direction. But ductility is exhausted more quickly with lower ε_u and ε_{Lf} with little localisation (2%). With increased porosity in the T2 and T3 rings ductility reduces more rapidly in the t direction.

3.6. Fracture surface morphology of fragmented rings

Light metallographic images of fracture surfaces for T1 and T3 rings at low magnification are displayed in Fig. 18. The T1 ring fracture surface (Fig. 18 (a)) does not display any large pores. The T3 ring displays numerous large pores between 25 and 72 μm diameter in which striations are visible on the surface of each pore. The rib-like feature on the surface of Ti-6Al-4 V was concluded to be a characteristic of keyhole porosity [41,56], and modelling of keyhole induced pores displayed similar surface striations in Ti-6Al-4 V [19]. It is unlikely these features developed in the keyhole pores during dynamic ring expansion. Although with tensile plastic deformation the large pores on the fracture surface would stretch from a more spherical to an elongated shape [57] aligned to the major axis (in the ring hoop direction), together with some lateral growth before fracture. The striations on the surface of the large pores in the T3 rings are a distinguishing feature of keyhole porosity in the LPBF IN718 alloy. Similar striations were observed in Ti-6Al-4 V (PD: 50 μm) [56] and was associated with increased turbulence in the melt pool which suggests a high energy density was applied. Kasperovich et al [41] mentioned that the features around each of the large pores contain sharp trenches that can act as stress concentrators. It was suggested they could have formed due to surface tension forces exerting a shear force on the liquid surface [58,59].

The largest PD identified in the T1 ring (Table 3) was 25 μm diameter which was fabricated under stable conduction melting and this cannot be a keyhole pore. Therefore, an appreciable portion of the distribution in the left tail of Fig. 9c may not be attributed to keyhole porosity.

T1 and T3 ring fracture surfaces at high magnification are displayed in Fig. 19 at the same scale. Fracture is transgranular for all ring samples. The fracture surfaces display a dimpled character associated with a ductile fracture. Many small sub-micron size pores can be observed in Fig. 19 (a and b) at the centre of a dimple. These may have developed from micro pores and nucleated from the second phase precipitates within the γ matrix that serve to impede dislocation slip. The dimples in the T1 ring are equiaxed typically from 1 to 5 μm across ligaments, and fracture was by tensile void coalescence [60–63]. The dimples identified in LPBF IN718 [28,43], in the as-built and unaged condition obtained from quasi-static uniaxial tensile testing, although equiaxed were smaller spanning submicron to a few microns. In the T1 fractograph a few long dimpled channels had coalesced which could be associated with a higher concentration of precipitates or grain boundaries. Some very small dimples which are just visible have nucleated within the ligaments of some larger dimples. This feature has been attributed to void sheeting with coalescence by shear [64] as a secondary instability stage preceding final fracture.

The dimples on the T2 fracture surface with PD 16 μm in Fig. 19 (b) are mainly equiaxed, smaller and shallower than the dimples in the T1 ring. Adjacent to the pore there are a small number of elliptical dimples. On the T3 fracture surface in Fig. 19 (c) the dimples adjacent to a pore with PD 37 μm, are extensively elliptical but become more equiaxed moving away from the pore. The dimples are considerably smaller and shallower than the T1 and T2 fracture surfaces confirming many smaller voids did not have the time to mature before coalescence and fracture. The fracture strain rate of the T3 ring was higher at 3.05×10^3 s^{-1} compared with 1.47×10^3 s^{-1} for T1. For the later there was a longer velocity deceleration phase because localization is more developed. In the lower right Fig. 19 which displays a thin wall between two large pores in the T3 ring, the dimples are comparatively smaller, shallower, and more numerous. Some micro voids have not developed into dimples at all.

The effect of void size on stress concentration and strain localisation was shown [65,66] to be important when the PD is larger than the local grain size (7-fold). Otherwise, grain size dominates the local stress field when pore to grain size ratio ≤ 1. Naragani et al (2020) [9,66] determined the stress triaxiality (η) using synchrotron X-ray measurements at the grain scale on a LPBF IN718 tensile test piece in the fully aged condition with two large internal pores (PD = 1/3 mm) fabricated under stable condition melting. The mean grain size was 48 μm. At the circumference of the two large pores there was a preference for low η (<1/3) and negative η, which promoted shear void coalescence. Similarly, shear void coalescence at the pore boundary was observed at high strain rate on the fracture surface in Fig. 18 (b). Remote from the two large pores there was a tendency for positive and higher η (>1/3) [9]. The latter promoted tensile void coalescence which was observed at high strain rate in Fig. 19(a), although with void sheeting due to secondary pore formation in ligament ridges. The character of the fracture surface between two large neighbouring keyhole pores in close proximity in the Fig. 19 (d) is distinctly different. A tearing coalescence mechanism may be active in which a microcrack propagated between micro voids [67] due to the high concentration of stress and strain in this region.

Fig. 20 displays the fracture strain (ε_{Af}) versus the average volumetric porosity fraction obtained for the T1, T2 and T3 rings. The equation of the fitted curve is a decaying power law:

$$\varepsilon Af(\Phi_P) = \lambda_1 \Phi_P{}^{\lambda_2} \quad (5)$$

Table 6
Fracture surface measurements obtained from Fig. 16.

	Unit	Equation	XY3	T1	T2	T3
t_i	mm	–	6.05	0.7	0.7	0.7
z_i	mm	–	4.18	1	1	1
A_i	mm^2	–	25.3	0.7	0.7	0.7
t_f	mm	–	5.22	0.53	0.6	0.67
z_f	mm	–	3.37	0.67	0.72	0.73
A_f	mm^2	–	17.6	0.36	0.43	0.49
ε_{Af}	mm/mm	$Ln(A_i/A_f)$	0.35	0.68	0.48	0.36
ε_{tf}	mm/mm	$Ln(t_i/t_f)$	0.15	0.28	0.15	0.04
ε_{zf}	mm/mm	$Ln(z_i/z_f)$	0.20	0.40	0.33	0.31
$\varepsilon_{zf}/\ \varepsilon_{tf}$	mm/mm	–	1.4	1.4	2.1	7.2
$\varepsilon_{tf} + \varepsilon_{zf}$	mm/mm	–	0.35	0.68	0.48	0.36

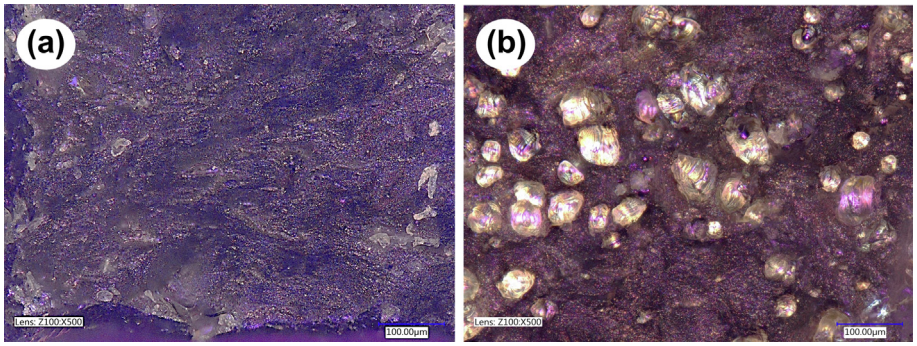

Fig. 18. Fracture surface at low magnification of T1 ring (a) and T3 ring (b).

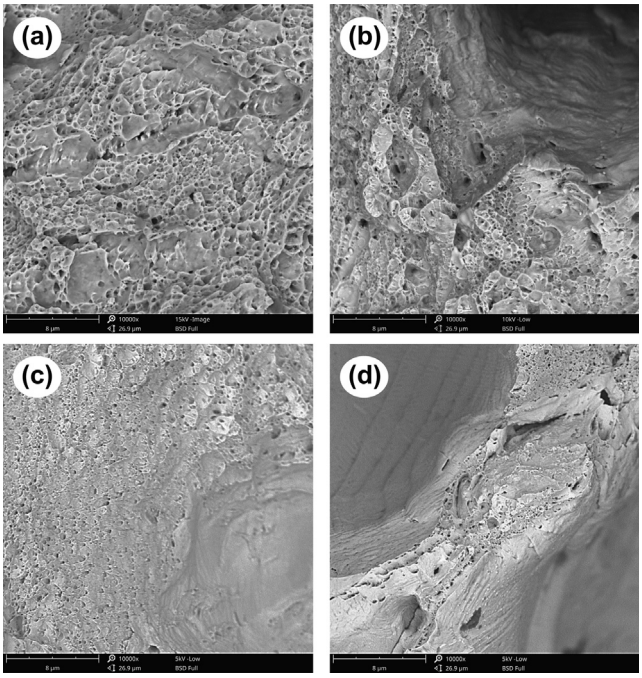

Fig. 19. SEM images of fractures surfaces at high magnification: T1 ring (a), T2 ring (b) T3 ring (c) and T3 ring (d).

(where Φ_P = porosity fraction and fitting coefficients λ_1 = 0.2 and λ_2 = 1.7)

Equation (5) also describes true strain (ε_u) at maximum uniform elongation versus average porosity, but with coefficientsλ_1 = 0.18 and λ_2 = 0.05. The strain rate effect on ε_u and ε_{Af} is also displayed for the XY sample in Fig. 20. Based on the aspect ratio of the undeformed ring cross section z_i/t_i (1/0.7), the results for true strain are a lower bound measure of material ductility (Zhang et. al., 2008).

Reviewing other works on the fracture behaviour of IN718 alloy [68] performed tests on aged hardened IN718 wrought product at strain rates between 1 and 10^3 s^{-1} and stress triaxiality (η) in the range 0.05–0.5. With η at 0.33 which is equivalent to a uniaxial tension test, ε_{Af} was approximately 0.4 and there was no discernible strain rate effect. The XY quasi-static uniaxial tension test result in this paper developed a slightly lower ε_{Af} at 0.35, whilst for the T1 rings ε_{Af} was significantly higher at 0.68. The positive strain rate effect on tensile ductility for the LPBF IN718 alloy can be explained by its relatively softened state in the as built and stress relieved condition.

4. Conclusions

Table 7 is a summary of the results obtained in this study.

An empirical model to predict porosity growth rates as a function of laser volume energy density (VED) containing two exponential growth terms was established. The model provided a general first order prediction of porosity type and growth rates spanning the unstable, stable and keyhole melting regions. The model enabled selection of the LPBF process parameters to fabricate the test pieces under stable conduction and keyhole melting suited to the machine type in this study. Three VEDs were selected is this study 74 J/mm^3 (200 W, 1000 mm/s), 139 J/mm^3 (175 W, 467 mm/s) and 167 J/mm^3 (175 W, 389 mm/s). The model is a good first approximation and can be calibrated to fit a region of specific interest.

Using LPBF, at high VED (167 J/mm^3), keyhole porosity was confirmed in ring samples distinguished by its character [PD: 63 μm; Porosity Fraction: 3.4% ± 0.6]. At lower VED within the stable conduction range distributions for pore area macro porosity were normal. At lower VED from 74 to 139 J/mm^3 modal pore diameter

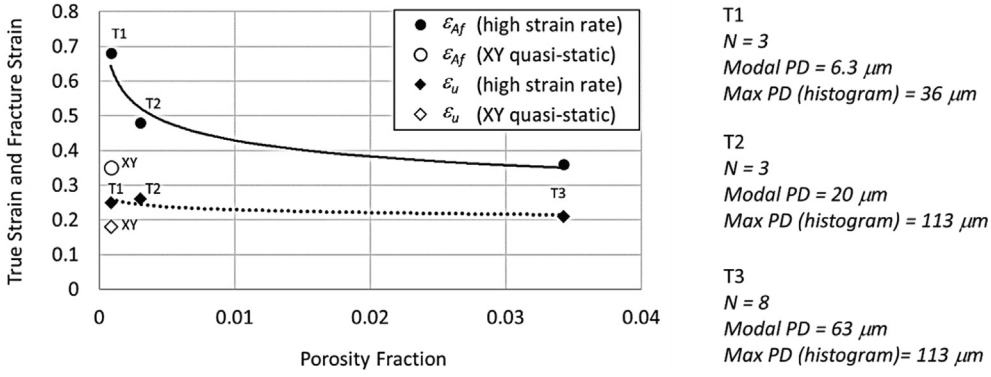

Fig. 20. Fracture strain and true strain versus porosity fraction.

Table 7
Summary of results

	Unit	Measuring instrument	XY	T1	T2	T3
VED (P, V)	J/mm^3 (W, mm/s)	–	74 (200, 1000)	74 (200, 1000)	139 (175, 467)	167 (175, 389)
Average porosity (fraction)	%	OM	–	0.1	0.3	3.4
Shape of PA distribution	–	Image J	–	Normal	Normal	Strong negative skew
Macro PD (mode)	μm	Histogram	–	6.3	20	63
Max PD (histogram)	μm	Image J	–	25 (36)	67 (113)	93 (113)
Macro pore shape	–	OM	–	Circular	Circular	Circular
Macro pore type	–	OM	–	Macro	Macro	Macro & Keyhole (with striations)
Micro pore shape	–	SEM	–	Circular	Circular	Circular
Micro PD	μm	SEM	–	< 5	< 5	< 5
Microhardness on horizontal build plane	$Hv_{0.2}$	Vickers hardness	–	299	314	293
Average N	–	Count	2	3	3	8
Max ε_u	mm/mm	Micrometer	0.18	0.25	0.26	0.21
Strain rate at max ε_u	s^{-1}	High speed camera	0.001	7.89E + 03	7.58E + 03	7.92E + 03
ε_{AF}	mm^2/mm^2	OM	0.35	0.68	0.48	0.36
Strain rate at ε_{AF}	s^{-1}	High speed camera	0.001	1.47E + 03	1.86E + 03	3.05E + 03
Fracture strain ratio R_f	–	ε_{tf} / ε_{zf}	1.4	1.4	2.1	7.2
Size of precipitates on horizontal build plane	μm	SEM	–	Needle & plate < 2	–	Needle & plate < 2
Precipitate concentration on horizontal build plane	wt (%)	EDS	–	Nb7.8, Ti1.2, Al0.8, Mo3.9	–	Nb7.5, Ti2.1, Al1.1, Mo4.2
Grain size on horizontal build plane	μm	OM	–	10–50	10–50	10–50
Dominant void coalesence modes	–	SEM	Tensile	Tensile	Tensile	Mixed

increased from 6.3 to 20 μm with corresponding total porosity fractions 0.1% and 0.3%. For VED 139 and 167 J/mm^3 a pore diameter of 113 μm was a maximum, and further increases in VED serve only to increase the number of larger pores but not their size.

On examining the alloy constitution in the test pieces obtained for three different laser energy densities on the horizontal build plane, with exception to the larger macro and keyhole pores, there was consistency in the microstructure and properties. Hence tensile ductility at high strain rate was associated with the pore characteristics in the test pieces, specifically the size, shape and fraction occupied.

The results of the ERET displayed high consistency for all LPBF rings tested with an average true tensile strain rate at peak velocity in the range 7.58–7.92 $\times$ 10^3 s^{-1}. At this high strain rate, the true strain at maximum uniform elongation for the ring with the lowest porosity was 39% higher than obtained under quasi-static strain rate (~10^{-3} s^{-1}), and 16% higher for the ring with the highest porosity. During ring deceleration strain rate at fracture increased with porosity from 1.47 $\times$ 10^3 to 3.05 $\times$ 10^3 s^{-1} because the time of localization reduced, and accordingly fracture strain reduced by almost 50%. The number of ring fragments obtained for the lowest sample porosities 0.1 and 0.3% were identical with an average 3. Whilst for the highest sample porosity of 3.4% the number of fragments increased to an average 8. The trend for reducing true strain and fracture strain with increasing porosity fraction at high strain rate was described by a decaying power law equation. Overall there was a significant positive strain rate effect on tensile ductility at lower porosities attributed to strain rate hardening in the alloy [1], that delayed the onset of localisation, and extended the time of localisation.

Anisotropy in material behaviour associated with build orientation influenced the uniformity of plastic strain with fracture strain ratio 1.4 for low porosity (at both low and high strain rate) and 7.2 for higher porosities at high strain rate. This suggested a tendency to a plane strain fracture in the horizontal build plane (ring thickness). Dimple sizes on fracture surfaces obtained at the highest porosity were appreciably smaller and shallower, confirming many smaller voids did not have the time to develop before coalescence. The high concentration of stress around large pores activated different void coalescence mechanisms in the material. Four mechanisms were identified at high strain rate, these are tensile void coalescence remote from a large pore, shear void coalescence at the pore boundary with void sheeting preceding local fracture, and void tear coalescence between two large neighbouring pores in close proximity.

CRediT authorship contribution statement

P. Wood: Conceptualization, Formal analysis, Investigation, Methodology, Supervision, Validation, Visualization, Writing - original draft, Writing - review & editing. **A. Rusinek:** Conceptualization, Formal analysis, Investigation, Methodology, Writing - review & editing. **P. Platek:** Investigation, Methodology, Visualization, Writing - review & editing. **J. Janiszewski:** Conceptualization, Formal analysis, Investigation, Methodology, Validation, Writing - review & editing, Project administration. **J. Sienkiewicz:** Formal analysis, Investigation. **U. F. Gunputh** Formal analysis, Investigation, Methodology, Validation, Visualization, Writing - original draft, Writing - review & editing. **K. Rajkowski:** Investigation. **M. H. Miguélez:** Writing - review & editing.

Declaration of Competing Interest

The authors declare that they have no known competing financial interests or personal relationships that could have appeared to influence the work reported in this paper.

Acknowledgements

The AM of IN718 and tensile testing was funded by the UoD, College of Science and Engineering Research Excellence Framework (REF) funding for the Director of IISE (P. Wood) and AM Researcher (U. Gunputh). The support of G. Williams for IN718 sample preparation and M. Pawlik for tensile testing is acknowledged. A. Rusinek acknowledges the program UC3M-Santander Chair of Excellence in additive manufacturing. The expanding ring tests investigations were funded by the Polish Ministry of Science and Higher Education, Centre for Research and Development under research grant No. TECHMATSTRATEG2/410049/12/NCBR/2019.

Appendix

Table A1
Porosity measurements over a range of LPBF processing conditions for IN718 obtained from the literature

VED range	Equivalent LED range	SLM process parameter	Measurement system	Relative porosity			*Max PD at high VED	*Min PD	*Max PA at low VED	Powder particle size range	SLM machine and laser type	Ref
J/mm^3	(J/m)	P, V, D, H		% (lowest)	% (highest for low VED)	% (highest for high VED)	μm	μm	μm^2	μm		
28.1 to 450	56.3 to 900	(90 W), (100 to 1600 mm/s), (25 μm), (80 μm)	OM	< 0.43% (VED = 60 to 150)	~ 13.8% (VED = 28.1) ~ 4.0% (VED = 37.5)	6.24% (VED = 450) 1.05% (VED = 220)	66	~ 10	~ 16,300 –	10 to 45	Concept Laser Mlab-Cusing system, 100 W continuous wave Yb:YAG laser, beam diameter of 110 μm, wavelength of 1075 nm	[23]
–	180–330	(110–130 W), (400–600 mm/s), (-), (-)	OM & A	1.6% (LED = 330)	26.4% (LED = 180)	–	–	–	~ 6800	15–45	IPG Photonics Yitterbium YLR-200-SM fibre laser, power 200 W, spot size of 70 μm	[42]
31.8–61.2	–	(150–450 W), (1000–1800 mm/s), (70 μm), (50–90 μm)	OM	0.48% (VED = 61.2)	1.35% (VED = 31.8)	–	–	~ 10 (~5 using SEM)	~ 1300	5–25	SLM machine DMP PROX300, YAG type laser, max power 450 W and spot diameter of 70 μm	[17]
29.5–231	200–925	(170–370 W), (500–1200 mm/s), (40 μm), (80–120 μm)	A	0.44% (VED = 96.4) <1% (VED between 53.1 and 143)	6.89% (VED = 29.5) –	2.24% (VED = 169) –	~ 85 (VED = 167)	~ 10 (VED = 167)	~ 2540	15–45	EoS M280, spot diameter of 100 μm	[25]
75.8–146	273–576	(300–400 W), (800–1100 mm/s), (30 μm), (110–130 μm)	–	0.48% (VED = 124) =< 0.72% (VED = 75.8–146)	– –	– –	– –	– –	– –	10–80	Farsoon 271 M SLM system	[43]
47.5–101		(-), (-), (30 mm), (-)	A	<0.6% (VED = 60–101)	1.1% (VED = 47.5)	–	–	–	–	–	SLM 280HL machine (SLM Solutions GmbH)	[22]
22.9–88.9	170–670	(600–1000 W), (1500–3000 mm/s), (50 μm), (150 μm)	A	<0.7% (VED = 62.2)	10.7% (VED = 22.9)	–	–	~ 10 (VED = 53.3)	~19,000	30 (mean stated)	SLM machine with 1 kW single mode fibre laser, spot diameter of 100 μm	[29]
74	297	(285 W), (960 mm/s), (40 μm), (100 μm)	μXCT	0.18%	–	–	17.8	2.6	–	35 (mean stated) in range 1–80	EOS M280 DMLM machine	[51]

References

[1] E.W. Hart, Theory of the tensile test, Acta Metall. 15 (2) (1967) 351–355, https://doi.org/10.1016/0001-6160(67)90211-8.
[2] S. Kaierle et al., Single-crystal turbine blade tip repair by laser cladding and remelting, CIRP J. Manuf. Sci. Technol. 19 (2017) 196–199, https://doi.org/10.1016/j.cirpj.2017.04.001.
[3] M. Gäumann et al., Single-crystal laser deposition of superalloys: processing–microstructure maps, Acta Mater. 49 (6) (2001) 1051–1062, https://doi.org/10.1016/s1359-6454(00)00367-0.
[4] A. Otubusin et al., Analysis of parameters influencing build accuracy of a SLM printed compressor outlet guide vane, in: ASME Turbo Expo 2018: Turbomachinery Technical Conference and Exposition, 2018, https://doi.org/10.1115/gt2018-75548.
[5] M. Wilcox, et al., GUIDELINE FOR GAS TURBINE INLET AIR FILTRATION SYSTEMS, Gas Machinery Research Council Southwest Research Institute: Online, 2010.
[6] I. Ulacia, High-speed forming of magnesium alloy sheets, Comprehens. Mater. Process. 3 (2014) 331–376, https://doi.org/10.1016/B978-0-08-096532-1.00319-8.
[7] C. Wang, R. Li, Effect of double aging treatment on structure in Inconel 718 alloy, J. Mater. Sci. 39 (7) (2004) 2593–2595, https://doi.org/10.1023/B:JMSC.0000020036.96777.9c.
[8] J.M. Oblak, D.F. Paulonis, D.S. Duvall, Coherency strengthening in Ni base alloys hardened by DO₂₂ γ' precipitates, Metall. Trans. 5 (1974) 143, https://doi.org/10.1007/bf02642938.
[9] D.P. Naragani et al., Void coalescence and ductile failure in IN718 investigated via high-energy synchrotron X-ray tomography and diffraction, J. Mech. Phys. Solids 145 (2020), https://doi.org/10.1016/j.jmps.2020.104155 104155.
[10] M.J. Donachie, S.J. Donachie, Superalloys: A Technical Guide, second ed., ASM International, 2002.
[11] R.C. Reed, Summary and future trends, in: The Superalloys, Cambridge University Press, Cambridge, 2006, pp. 351–362.
[12] C.T. Sims, N.S. Stoloff, W.C. Hagel, Superalloys II: [high-temperature materials for aerospace and industrial power], John Wiley & Sons, New York [etc.], 1987.
[13] M.D. Sangid et al., Role of heat treatment and build orientation in the microstructure sensitive deformation characteristics of IN718 produced via SLM additive manufacturing, Addit. Manuf. 22 (2018) 479–496, https://doi.org/10.1016/j.addma.2018.04.032.
[14] N.T. Aboulkhair et al., Reducing porosity in AlSi10Mg parts processed by selective laser melting, Addit. Manuf. 1–4 (2014) 77–86, https://doi.org/10.1016/j.addma.2014.08.001.
[15] D. Zhang et al., Comparison of microstructures and mechanical properties of Inconel 718 alloy processed by selective laser melting and casting, Mater. Sci. Eng., A 724 (2018) 357–367, https://doi.org/10.1016/j.msea.2018.03.073.
[16] U. Ali et al., On the measurement of relative powder-bed compaction density in powder-bed additive manufacturing processes, Mater. Des. 155 (2018) 495–501, https://doi.org/10.1016/j.matdes.2018.06.030.
[17] K. Moussaoui et al., Effects of Selective Laser Melting additive manufacturing parameters of Inconel 718 on porosity, microstructure and mechanical properties, Mater. Sci. Eng., A 735 (2018) 182–190, https://doi.org/10.1016/j.msea.2018.08.037.
[18] S.A. Khairallah et al., Laser powder-bed fusion additive manufacturing: Physics of complex melt flow and formation mechanisms of pores, spatter, and denudation zones, Acta Mater. 108 (2016) 36–45, https://doi.org/10.1016/j.actamat.2016.02.014.
[19] M. Bayat et al., Keyhole-induced porosities in Laser-based Powder Bed Fusion (L-PBF) of Ti6Al4V: High-fidelity modelling and experimental validation, Addit. Manuf. 30 (2019), https://doi.org/10.1016/j.addma.2019.100835.
[20] P.A. Hooper, Melt pool temperature and cooling rates in laser powder bed fusion, Addit. Manuf. 22 (2018) 548–559, https://doi.org/10.1016/j.addma.2018.05.032.
[21] D. Zhang et al., Effect of standard heat treatment on the microstructure and mechanical properties of selective laser melting manufactured Inconel 718 superalloy, Mater. Sci. Eng., A 644 (2015) 32–40, https://doi.org/10.1016/j.msea.2015.06.021.
[22] A.A. Popovich et al., Design and manufacturing of tailored microstructure with selective laser melting, Mater. Phys. Mech. 38 (2018) 1–10, https://doi.org/10.18720/MPM.3812018_1.
[23] J.-P. Choi et al., Densification and microstructural investigation of Inconel 718 parts fabricated by selective laser melting, Powder Technol. 310 (2017) 60–66, https://doi.org/10.1016/j.powtec.2017.01.030.
[24] W. Zhang et al., Three-dimensional ordered macroporous nano-architecture and its enhancing effects on Raman detection sensitivity for Eosin Y molecules, Mater. Des. 119 (2017) 456–463, https://doi.org/10.1016/j.matdes.2017.01.090.
[25] M. Balbaa et al., On selective laser melting of Inconel 718: Densification, surface roughness, and residual stresses, Mater. Des. 193 (2020), https://doi.org/10.1016/j.matdes.2020.108818 108818.
[26] R. Rai et al., Heat transfer and fluid flow during keyhole mode laser welding of tantalum, Ti–6Al–4V, 304L stainless steel and vanadium, J. Phys. D Appl. Phys. 40 (18) (2007) 5753–5766, https://doi.org/10.1088/0022-3727/40/18/037.
[27] H. Gong et al., Influence of defects on mechanical properties of Ti–6Al–4V components produced by selective laser melting and electron beam melting, Mater. Des. 86 (2015) 545–554, https://doi.org/10.1016/j.matdes.2015.07.147.
[28] Z. Wang et al., The microstructure and mechanical properties of deposited-IN718 by selective laser melting, J. Alloy. Compd. 513 (2012) 518–523, https://doi.org/10.1016/j.jallcom.2011.10.107.
[29] Y. Tachibana et al., Selective laser melting of Inconel 718 under high power and high scanning speed conditions, Mater. Sci. Forum 941 (2018) 1574–1578, https://doi.org/10.4028/www.scientific.net/MSF.941.1574.
[30] I. Yadroitsev et al., Single track formation in selective laser melting of metal powders, J. Mater. Process. Technol. 210 (12) (2010) 1624–1631, https://doi.org/10.1016/j.jmatprotec.2010.05.010.
[31] W.E. King et al., Observation of keyhole-mode laser melting in laser powder-bed fusion additive manufacturing, J. Mater. Process. Technol. 214 (12) (2014) 2915–2925, https://doi.org/10.1016/j.jmatprotec.2014.06.005.
[32] R. Cunningham et al., Synchrotron-based X-ray microtomography characterization of the effect of processing variables on porosity formation in laser power-bed additive manufacturing of Ti-6Al-4V, Jom 69 (3) (2017) 479–484, https://doi.org/10.1007/s11837-016-2234-1.
[33] B. Zhang, Y. Li, Q. Bai, Defect formation mechanisms in selective laser melting: a review, Chinese J. Mech. Eng. 30 (3) (2017) 515–527, https://doi.org/10.1007/s10033-017-0121-5.
[34] T. DebRoy et al., Additive manufacturing of metallic components – Process, structure and properties, Prog. Mater Sci. 92 (2018) 112–224, https://doi.org/10.1016/j.pmatsci.2017.10.001.
[35] J. Elmer et al., The effect of Ar and N-2 shielding gas on laser weld porosity in steel, stainless steels, and nickel, Weld. J. 94 (2015) 313s–325s.
[36] W. Tillmann et al., Hot isostatic pressing of IN718 components manufactured by selective laser melting, Addit. Manuf. 13 (2017) 93–102, https://doi.org/10.1016/j.addma.2016.11.006.
[37] A.A. Martin et al., Dynamics of pore formation during laser powder bed fusion additive manufacturing, Nat. Commun. 10 (1) (2019) 1987, https://doi.org/10.1038/s41467-019-10009-2.
[38] S. Shrestha, T. Starr, K. Chou, A study of keyhole porosity in selective laser melting: single-track scanning with micro-CT analysis, J. Manuf. Sci. Eng. 141 (7) (2019), https://doi.org/10.1115/1.4043622.
[39] L. Scime, J. Beuth, Melt pool geometry and morphology variability for the Inconel 718 alloy in a laser powder bed fusion additive manufacturing process, Addit. Manuf. 29 (2019), https://doi.org/10.1016/j.addma.2019.100830 100830.
[40] T. Vilaro, C. Colin, J.D. Bartout, As-fabricated and heat-treated microstructures of the Ti-6Al-4V alloy processed by selective laser melting, Metall. Mater. Trans. A 42 (10) (2011) 3190–3199, https://doi.org/10.1007/s11661-011-0731-y.
[41] G. Kasperovich et al., Correlation between porosity and processing parameters in TiAl6V4 produced by selective laser melting, Mater. Des. 105 (2016) 160–170, https://doi.org/10.1016/j.matdes.2016.05.070.
[42] Q. Jia, D. Gu, Selective laser melting additive manufacturing of Inconel 718 superalloy parts: densification, microstructure and properties, J. Alloy. Compd. 585 (2014) 713–721, https://doi.org/10.1016/j.jallcom.2013.09.171.
[43] M. Ni et al., Anisotropic tensile behavior of in situ precipitation strengthened Inconel 718 fabricated by additive manufacturing, Mater. Sci. Eng., A 701 (2017) 344–351, https://doi.org/10.1016/j.msea.2017.06.098.
[44] F.I. Niordson, A unit for testing materials at high strain rates, Exp. Mech. 5 (1) (1965) 29–32, https://doi.org/10.1007/bf02320901.
[45] D.E. Grady, D.A. Benson, Fragmentation of metal rings by electromagnetic loading, Exp. Mech. 23 (4) (1983) 393–400, https://doi.org/10.1007/bf02330054.
[46] A. Pandolfi, P. Krysl, M. Ortiz, Finite element simulation of ring expansion and fragmentation: the capturing of length and time scales through cohesive models of fracture, Int. J. Fract. 95 (1/4) (1999) 279–297, https://doi.org/10.1023/a:1018672922734.
[47] W.H. Gourdin, Analysis and assessment of electromagnetic ring expansion as a high-strain-rate test, J. Appl. Phys. 65 (2) (1989) 411–422, https://doi.org/10.1063/1.343121.
[48] J. Janiszewski, W. Pichola, Development of electromagnetic ring expansion apparatus for high-strain-rate test, Solid State Phenom. 147–149 (2009) 645–650, https://doi.org/10.4028/www.scientific.net/SSP.147-149.645.
[49] J. Janiszewski, Ductility of selected metals under electromagnetic ring test loading conditions, Int. J. Solids Struct. 49 (7–8) (2012) 1001–1008, https://doi.org/10.1016/j.ijsolstr.2012.01.005.
[50] D. Pitassi, et al., Finite Element Thermal Analysis of Metal Parts Additively Manufactured via Selective Laser Melting, in Finite Element Method - Simulation, Numerical Analysis and Solution Techniques, 2018.
[51] S. Gribbin et al., Role of grain structure, grain boundaries, crystallographic texture, precipitates, and porosity on fatigue behavior of Inconel 718 at room and elevated temperatures, Mater. Charact. 149 (2019) 184–197, https://doi.org/10.1016/j.matchar.2019.01.028.
[52] Renishaw, In718-0405 powder for additive manufacturing (AM250), 2017.
[53] W.H. Gourdin, S.L. Weinland, R.M. Boling, Development of the electromagnetically launched expanding ring as a high-strain-rate test technique, Rev. Sci. Instrum. 60 (3) (1989) 427–432, https://doi.org/10.1063/1.1140395.
[54] T. Trosch et al., Microstructure and mechanical properties of selective laser melted Inconel 718 compared to forging and casting, Mater. Lett. 164 (2016) 428–431, https://doi.org/10.1016/j.matlet.2015.10.136.
[55] A. Mostafa et al., Structure, texture and phases in 3D printed IN718 alloy subjected to homogenization and HIP treatments, Metals 7 (6) (2017) 196, https://doi.org/10.3390/met7060196.

[56] C. Qiu, N.J.E. Adkins, M.M. Attallah, Microstructure and tensile properties of selectively laser-melted and of HIPed laser-melted Ti–6Al–4V, Mater. Sci. Eng., A 578 (2013) 230–239, https://doi.org/10.1016/j.msea.2013.04.099.
[57] A. Weck et al., Visualization by X-ray tomography of void growth and coalescence leading to fracture in model materials, Acta Mater. 56 (12) (2008) 2919–2928, https://doi.org/10.1016/j.actamat.2008.02.027.
[58] K.A. Mumtaz, N. Hopkinson, Selective Laser Melting of thin wall parts using pulse shaping, J. Mater. Process. Technol. 210 (2) (2010) 279–287, https://doi.org/10.1016/j.jmatprotec.2009.09.011.
[59] J.A. Ramos, D.L. Bourell, J.J. Beaman, Surface over-melt during laser polishing of indirect-SLS metal parts, MRS Proc. 758 (2011), https://doi.org/10.1557/proc-758-ll1.9.
[60] C.D. Beachem, The effects of crack tip plastic flow directions upon microscopic dimple shapes, Metall. Trans. A 6 (2) (1975) 377–383, https://doi.org/10.1007/bf02667293.
[61] F.A. McClintock, A criterion for ductile fracture by the growth of holes, J. Appl. Mech. 35 (2) (1968) 363–371, https://doi.org/10.1115/1.3601204.
[62] A.L. Gurson, Continuum theory of ductile rupture by void nucleation and growth: Part I—yield criteria and flow rules for porous ductile media, J. Eng. Mater. Technol. 99 (1) (1977) 2–15, https://doi.org/10.1115/1.3443401.
[63] P.F. Thomason, A three-dimensional model for ductile fracture by the growth and coalescence of microvoids, Acta Metall. 33 (6) (1985) 1087–1095, https://doi.org/10.1016/0001-6160(85)90202-0.
[64] T. Pardoen, J.W. Hutchinson, An extended model for void growth and coalescence, J. Mech. Phys. Solids 48 (12) (2000) 2467–2512, https://doi.org/10.1016/s0022-5096(00)00019-3.
[65] J.D. Carroll et al., The effect of grain size on local deformation near a void-like stress concentration, Int. J. Plast. 39 (2012) 46–60, https://doi.org/10.1016/j.ijplas.2012.06.002.
[66] C.C. Battaile et al., Crystal plasticity simulations of microstructure-induced uncertainty in strain concentration near voids in brass, Phil. Mag. 95 (10) (2015) 1069–1079, https://doi.org/10.1080/14786435.2015.1009958.
[67] C. Tekoglu, J.W. Hutchinson, T. Pardoen, On localization and void coalescence as a precursor to ductile fracture, Philos. Trans. A Math. Phys. Eng. Sci. 373 (2038) (2015) 20140121, https://doi.org/10.1098/rsta.2014.0121.
[68] T. Sjöberg, J. Kajberg, M. Oldenburg, Fracture behaviour of Alloy 718 at high strain rates, elevated temperatures, and various stress triaxialities, Eng. Fract. Mech. 178 (2017) 231–242, https://doi.org/10.1016/j.engfracmech.2017.04.036.